PAPER

Seasonal manganese transport in the hyporheic zone of a snowmelt-dominated river (East River, Colorado, USA)

Savannah R. Bryant[1] · Audrey H. Sawyer[1] · Martin A. Briggs[2] · Casey M. Saup[1] · Amelia R. Nelson[1] · Michael J. Wilkins[3] · John N. Christensen[4] · Kenneth H. Williams[4,5]

Abstract

Manganese (Mn) plays a critical role in river-water quality because Mn-oxides serve as sorption sites for contaminant metals. The aim of this study is to understand the seasonal cycling of Mn in an alpine streambed that experiences large spring snowmelt events and the potential responses to changes in snowmelt timing and magnitude. To address this goal, annual variations in river-water/groundwater interaction and $Mn_{(aq)}$ transport were measured and modeled in the bed of East River, Colorado, USA. In observations and numerical models, oxygenated river water containing dissolved organic carbon (DOC) mixes with groundwater rich in $Mn_{(aq)}$ in the streambed. The mixing depth increases during spring snowmelt when river discharge increases, leading to a greater DOC supply to the hyporheic zone and net respiration of Mn-oxides, despite an enhanced supply of oxygen. As groundwater upwelling resumes during the subsequent baseflow period, $Mn_{(aq)}$-rich groundwater mixes with oxygenated river water, resulting in net accumulation of Mn-oxides until the bed freezes in winter. To explore potential responses of Mn transport to different climate-induced hydrological regimes, three hydrograph scenarios were numerically modeled (historic, low-snow, and storm) for the Rocky Mountain region. In a warming climate, $Mn_{(aq)}$ export to the river decreases, and $Mn_{(aq)}$ oxidation is favored in the upper streambed sediments over more of the year. One important implication is that the streambed may have an increased sorption capacity for metals over more of the year, leading to potential changes in river-water quality.

Keywords Manganese · Solute transport · Hyporheic · Numerical modeling · Heat tracing

Introduction

In alluvial rivers, substantial surface water and groundwater exchange can occur in shallow, permeable bed sediments, promoting biogeochemical reactions that impact watershed reactivity (Boano et al. 2014; Boulton et al. 1998). The hyporheic zone, where river water and groundwater mix, disproportionately influences nutrient cycling (Mulholland and DeAngelis 2000; Triska et al. 1989, 1993) and contaminant fate and transport (Manamsa et al. 2016; Weatherill et al. 2018; Xu et al. 2017). Hyporheic zones provide surface area for microbial attachment and function (Feris et al. 2003; Fischer et al. 2005), and hyporheic flow delivers a mixture of potentially limiting reactants from river water and groundwater. The mixing of these chemically distinct waters in the presence of active microbial communities makes hyporheic zones particularly efficient bioreactors compared to the open channel (Baxter and Hauer 2000; Hester et al. 2017; Peralta-Maraver et al. 2018; Stanford and Ward 1988).

Microbial respiration involves the oxidation of an electron donor such as an organic carbon compound, coupled to reduction of a terminal electron acceptor (TEA), at least partly based on thermodynamic favorability (Jin and Bethke 2003; LaRowe and Van Cappellen 2011). In hyporheic zones, river

✉ Savannah R. Bryant
srbryant@ncsu.edu

1   The Ohio State University, School of Earth Sciences, Columbus, OH, USA

2   US Geological Survey, Earth System Processes Division, Hydrogeophysics Branch, Storrs, CT, USA

3   Department of Soil and Crop Sciences, Colorado State University, Fort Collins, CO, USA

4   Lawrence Berkeley National Laboratory, Berkeley, CA, USA

5   Rocky Mountain Biological Laboratory, Gothic, CO, USA

water can be a source of dissolved oxygen (DO), the most energetically favorable TEA; however, streambed sediments can be a source of other electron acceptors such as solid phase manganese (Mn) and iron (Fe) when DO is depleted, leading to vertical gradients in redox reactions in streambeds (Fig. 1). When DO is available, microbial oxidation of reduced metals such as $Mn_{(aq)}$ (acting as an electron donor) may be thermodynamically favorable (Butler et al. 2008; Harvey and Fuller 1998; Robbins and Corley 2005). In addition to microbial oxidation, Mn-oxides can also precipitate abiotically (Diem and Stumm 1984; Emerson 2000), but microbial oxidation tends to dominate (Fuller and Bargar 2014; Harvey and Fuller 1998; Kay et al. 2001). Microbial oxidation rates of $Mn_{(aq)}$ are pH-dependent, but generally increase with availability of DO, $Mn_{(aq)}$, and Mn-oxidizing microbial biomass (Fuller and Bargar 2014; Fuller and Harvey 2000; Hem 1981; Robbins and Corley 2005).
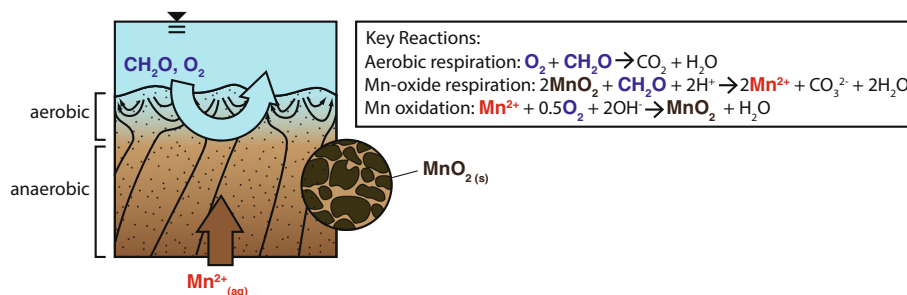
Mn-oxides play an important role in adsorbing other contaminant metals such as nickel, cobalt, copper, zinc, and lead (Fuller and Bargar 2014; Fuller and Harvey 2000). In a headwater field tracer study in Arizona, Fuller and Harvey (2000) concluded that dissolved heavy metals in stream water were attenuated by adsorption onto Mn-oxides in the hyporheic zone. Kay et al. (2001) conducted a column study using sediments from the same contaminated streambed and found that $Mn_{(aq)}$, cobalt, and nickel adsorbed to Mn-oxides, although the reversibility of this adsorption varied with each metal. Further batch experiments showed that zinc attenuation was controlled by Mn-oxide formation under near-neutral pH conditions (Fuller and Bargar 2014). Furthermore, Schaffner et al. (2015) effectively demonstrated that enriching acidic streams with Mn-oxides and hydroxides could be a cost-efficient means of remediating heavy metals such as cadmium, cobalt, nickel, and zinc.

Seasonal changes in hyporheic exchange can alter Mn-oxide stability via changes in river-water/groundwater mixing and the supply of DO, $Mn_{(aq)}$, and dissolved organic carbon (DOC) to microbial communities (Battin 1999; Fellman et al. 2009; Wong and Williams 2009; Fig. 1). In snowmelt-dominated rivers, large seasonal variations in stream discharge and dissolved chemical concentrations occur, from low discharge during late summer and fall to high discharge during

spring snowmelt (Cameron 1996). Up to 60% of the organic carbon flux delivered to alpine rivers occurs during spring (Raymond et al. 2007, 2016; Spencer et al. 2009), which can stimulate microbial respiration and metal processing in the hyporheic zone. Baalousha et al. (2018) noted that concentrations of trace elements such as $Fe_{(aq)}$ and $Mn_{(aq)}$ declined in an alpine stream during spring snowmelt compared to baseflow conditions, indicative of a combination of retention in the streambed and dilution. As stream discharge increases during snowmelt, hyporheic mixing may extend deeper into the streambed due to higher stage, greater shear stresses, and sediment mobilization, and groundwater flow may reverse, transporting stream-derived oxygen, carbon, and metals to greater depths where they can react (Boulton et al. 1998; Harvey and Fuller 1998; Harvey et al. 2003; O'Connor and Harvey 2008).

Many upland headwater catchments such as those in the Rocky Mountains of the western United States (US), are experiencing accelerated rates of climate change (Harte et al. 2015; Pederson et al. 2011). Under future scenarios, snow pack thickness and duration are predicted to decrease (Mann et al. 2012), and spring snowmelt is expected to occur earlier in the year (Stone et al. 2002). Long-term decreases in snow pack thickness and annual runoff will impact river-water/groundwater exchange (Cameron 1996; Mann et al. 2012; Wondzell 2011), carbon mineralization (Fellman et al. 2009; Holmes et al. 2012b; Spencer et al. 2008, 2009), metal oxidation (Butler et al. 2008; Harvey and Fuller 1998; Robbins and Corley 2005), and microbial community function and dynamics (Baker et al. 1999; Battin 1999; Hopkinson et al. 1998). Specifically, Striegl et al. (2005) predicted that DOC export will decrease disproportionately with declining stream flow as a result of increased microbial processing as solute residence times increase. Solute exchange across the sediment–water interface may also decrease, which may limit the oxidation of $Mn_{(aq)}$ (Butler et al. 2008; Robbins and Corley 2005; Spencer et al. 2008). A longer baseflow season is expected to result in a prolonged period of upwelling groundwater-dominated river flow, which may promote reducing conditions in the streambed and further limit oxidation at depth (Battin 1999; Cardenas and Wilson 2007). As hyporheic exchange potentially decreases with diminishing stream flow

Fig. 1 Conceptual schematic of reactions governing Mn transformation within the streambed. Here, CH_2O is used to represent DOC

Key Reactions:
Aerobic respiration: $O_2 + CH_2O \rightarrow CO_2 + H_2O$
Mn-oxide respiration: $2MnO_2 + CH_2O + 2H^+ \rightarrow 2Mn^{2+} + CO_3^{2-} + 2H_2O$
Mn oxidation: $Mn^{2+} + 0.5O_2 + 2OH^- \rightarrow MnO_2 + H_2O$

and the DO supply from river water declines, it remains unclear how the hyporheic zone will function in retaining metal oxides.

The goal of this study was to understand seasonal changes in Mn transport within an alpine hyporheic zone (Fig. 1) and explore potential responses to changing hydrograph scenarios. To accomplish this goal, vertical seepage rates were monitored over profiles in an alluvial streambed using temperature sensing, and seasonal profiles of pore-water chemistry were collected from August 2016 through August 2017. Field observations were used to develop a one-dimensional (1D) reactive transport model to simulate seasonal changes in Mn transport. Three potential scenarios of annual river and hyporheic flow dynamics were then modeled to test the influence on Mn mobility and transport. Results show that larger snowmelt events enhance Mn-oxide respiration and reductive dissolution in the shallow streambed due to deeper penetration of DOC from river water. Conversely, a longer baseflow season and smaller snowmelt event limits the supply of DOC from river water and increases the supply of $Mn_{(aq)}$ from groundwater leading to a greater rate of Mn oxidation in the shallow hyporheic zone.

Methods

A combination of field measurements and 1D numerical reactive transport models were used to understand seasonal changes in Mn transport in the bed of the East River. A description of the field site is presented in the following, as well as field and numerical approaches.

Field site

The East River is an alpine stream that lies within the Gunnison River Basin in the southern Rocky Mountains of Colorado (Fig. 2). Elevation of the watershed ranges from approximately 2,445 to 4,100 m (Liu et al. 2016), and most precipitation falls in the form of snow (Winnick et al. 2017). Snowmelt is the primary source of runoff to the East River, with peak discharge occurring between the months of May and July (Fig. 3). Baseflow conditions prevail from August until the bed freezes in winter. The East River watershed is mostly undeveloped, apart from the city of Crested Butte and the ski resort area (Spahr et al. 2000; Theobald et al. 1996). The catchment is largely underlain by the Cretaceous Mancos Shale Formation, which mainly consists of gray siltstone and shale (Morrison et al. 2012) and by early Tertiary granitic intrusions as well as Paleozoic and Mesozoic sedimentary rocks (Gaskill et al. 1991). The Mancos Shale is overlain by Quaternary glacial and alluvial sediments, and crops out in several places along the East River corridor at river cutbanks (Pai et al. 2017).

The study site lies northeast of Crested Butte (Fig. 2). Water samples were collected at three locations, A, B, and C, around a characteristic meander of the East River floodplain (Winnick et al. 2017). The site elevation is 2,760 m, and the approximate channel slope is 0.008 in the area of the meander. The streambed at the site is primarily composed of gravel (Nelson et al. 2019), with calcium-rich plagioclase feldspar and carbonate clasts.

Estimating seepage fluxes using temperature time series

Heat was used as a tracer to quantify seasonal changes in vertical Darcy velocity through the streambed. Arrays of four temperature sensors (Onset HOBO TMC20-HD) were mounted on wooden stakes and driven into the streambed at locations A, B, and C in August 2016 (Fig. 2). Stakes were installed to position sensors 5, 10, 20, and 35 cm below the sediment–water interface. Temperature was recorded every 15 min using HOBO U-Series external-channel data loggers through August 2017. Changes in flow and bed movement occasionally dislodged sensors, inhibiting their use in heat tracing until they could be reinstalled. Data from the deepest three sensors (10, 20, and 35 cm) were utilized for most locations and times because they remained undisturbed over longer intervals. However, the shallowest three probes were used for location A for 21 August 2016 through 11 May 2017 due to a faulty connection that compromised data collection at the deepest sensor—at least three temperature time series are needed for numerical analysis using the 1DTempPro software (Koch et al. 2015).

The computer program 1DTempPro was used to determine a best-fit (optimized) vertical Darcy velocity (q) over 1-week intervals beginning every 3 days, such that there was overlap for periods of q estimation. Although 1DTempPro allows for time-variable estimates of q, automated vertical fluid flux optimization can only be run for steady-state periods, which is why temperature records were divided into 1-week intervals. 1DTempPro solves the 1D heat transfer equation in porous media:

$$\frac{\partial T}{\partial t} = K_e \frac{\partial^2 T}{\partial z^2} - q \frac{C_w}{C} \frac{\partial T}{\partial z} \tag{1}$$

where T is temperature, t is time, z is depth below the sediment–water interface, K_e is the effective thermal diffusivity of the saturated sediment, q is Darcy velocity, and C_w and C are the volumetric heat capacities of the water and saturated sediment, respectively (Lapham 1989). K_e is defined as:

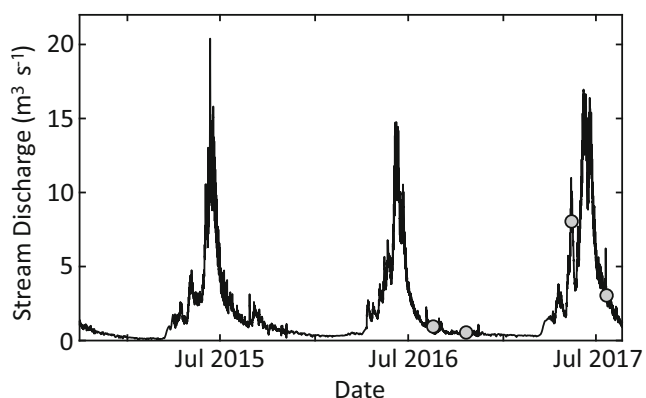$$K_e = \frac{\lambda_0}{C} + \beta \left(\frac{C_w |q|}{C} \right) \tag{2}$$

where λ_0 is thermal conductivity of the bulk saturated medium, and β is thermal dispersivity (Lapham 1989). Temperature
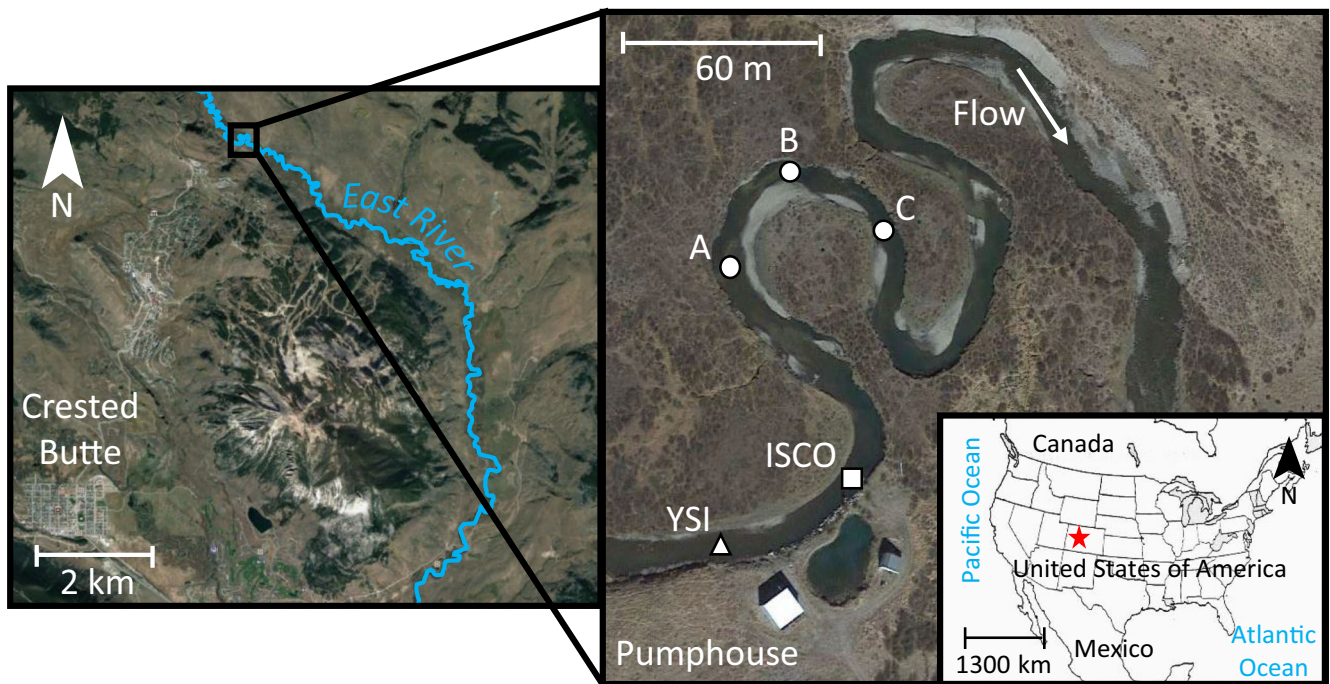
Fig. 2 Aerial image of East River study site (38.923541, –106.951007). A, B, and C denote locations of temperature monitoring and geochemical sampling in 2016 and 2017. Daily average discharge is monitored near the 'Pumphouse' location. The YSI and ISCO sampler are maintained by the Lawrence Berkeley National Laboratory

signals at 10 and 35 cm were used as boundary conditions in 1DTempPro, while the 1D model was optimized for the temperature signal at 20 cm by automatically determining the best fitting q. Values for q are reported opposite of the sign convention used in 1DTempPro: upwelling is positive and downwelling is negative. All weeks where the streambed was frozen were excluded from this analysis, as 1DTempPro does not represent the effects of phase changes, and vertical flow was likely minimal. The streambed was designated as frozen when greater than 75% of the temperature readings from one or more depths for a 1-week period were less than 0.15 °C.

Thermal properties of the streambed (Table 1) were generally estimated with a variety of approaches detailed in the electronic supplementary material (ESM). In brief, C and λ_0 were determined for a repacked sediment sample with the aid of a KD2 Pro Thermal Properties Analyzer (Decagon Devices, Inc., WA, USA). K_e (and thus β) was determined from further heat tracing analysis using the VFLUX2 program (Gordon et al. 2012; Irvine et al. 2015).

Field methods and chemical analysis

Pore-water samples were obtained from locations A, B, and C (Fig. 2) during four field efforts on 19 August 2016, 21–23 October 2016, 15–16 May 2017, and 22 July 2017 (Fig. 3). Samples were obtained at 10-cm intervals using a 0.25-inch diameter, stainless steel sipper with a 2-inch screen (MHE

Fig. 3 Stream discharge for East River from 1 Oct. 2014 through 21 Aug. 2017 measured at the Pumphouse (Carroll and Williams 2019; Fig. 2). Grey circles represent field sampling campaigns conducted 19 Aug. 2016, 21–23 Oct. 2016, 15–16 May 2017, and 22 Jul. 2017

Table 1 Parameters used in heat tracing. Mean values were used in 1DTempPro to estimate q. Standard deviations (SD) were also used in Monte Carlo analysis in VFLUX to determine error bars for q estimates

Parameter	Mean	SD	Units
n	0.27	0.027	–
β	0.01	0.0075	m
λ_0	1.86	0.00267	J s^{-1} m^{-1} K^{-1}
C_s	1,872,000	32,600	J m^{-3} K^{-1}
C_w	4,184,000	5,000	J m^{-3} K^{-1}

Products, MI, USA) attached to a syringe (MHE Products, MI, USA). The maximum sampling depth was generally 60 cm but varied due to challenges with penetration around large cobbles. Prior to each sample collection, 30 ml of pore water was extracted and discarded to purge the full sipper volume. Samples were filtered through a 0.22-µm Sterivex filter (MilliporeSigma, Massachusetts, USA) and immediately analyzed for DO concentration using a field spectrometer (CHEMetrics Inc., VA, USA). Because the method briefly exposed the sample to the atmosphere, measured concentrations represent a maximum, upper bound on in-situ DO concentrations. Measured DO concentrations in this study and two others that used the same method (Nelson et al. 2019; Wallace 2019) were never less than 0.0625 mM, which is here considered to be the practical detection limit for the method. Basic water quality parameters (pH, specific conductance, total dissolved solids, resistivity, oxidation-reduction potential) were measured in the field using a handheld multiparameter probe (Ultrameter II, Myron L Company, CA, USA). Two 20-ml filtered aliquots were collected from each sampling depth and location in a polyethylene vial and placed on ice until transfer to a freezer. Samples were kept frozen until analysis. One set of the aliquots was acidified in the field and was used for cation analysis using a PerkinElmer ELAN 6000 ICP-Mass Spectrometer. The other set of aliquots was used for strontium isotope analysis using a Triton Series Multicollector Thermal Ionization Mass Spectrometer (TIMS; ThermoFisher Scientific). More details on analysis methods are provided in Saup et al. (2019).

To augment the four sampling campaigns, a full year of river-water specific conductance and DOC records were obtained from the East River Data Portal (Berkeley Lab 2019). Samples and measurements were obtained near the Pumphouse using a Yellow Springs Instrument (YSI) and Teledyne ISCO sampler (Fig. 4q,u) as part of the Lawrence Berkeley National Laboratory (LBNL) Watershed Function Scientific Focus Area (SFA). Stage height and stream discharge were obtained from Carroll and Williams (2019; Fig. 4a).

Reactive transport model

Conservative and reactive solute transport were simulated for a 1D "slab" of streambed sediment with thickness of 1 m positioned such that the top of the domain is at the sediment–water interface and represents river water. Specific conductance was chosen to represent a conservative "solute" in the unsteady advection-dispersion equation:

$$\frac{\partial C}{\partial t} = -v(t)\frac{\partial C}{\partial z} + D(z,t)\frac{\partial^2 C}{\partial z^2} \tag{3}$$

where C is concentration (here, taken as specific conductance, SpC), t is time, z is depth below the streambed interface, $v(t)$ is average seepage velocity (Darcy velocity, q, divided by porosity), and $D(z,t)$ is effective dispersion. The unsteady 1D advection-dispersion-reaction equations were used to represent transport of DO, $Mn_{(aq)}$, and DOC:

$$\frac{\partial C_{DO}}{\partial t} = -v(t)\frac{\partial C_{DO}}{\partial z} + D(z,t)\frac{\partial^2 C_{DO}}{\partial z^2} - \beta_{ar,DO}V_{ar}X_{ar}\left(\frac{C_{DO}}{K_{DO}+C_{DO}}\right)\left(\frac{C_{DOC}}{K_{DOC}+C_{DOC}}\right)$$
$$-\beta_{MnOx,DO}V_{MnOx}X_{MnOx}\left(\frac{C_{DO}}{K_{DO}+C_{DO}}\right)\left(\frac{C_{Mn(aq)}}{K_{MnOx}+C_{Mn(aq)}}\right) \tag{4}$$

$$\frac{\partial C_{Mn(aq)}}{\partial t} = -v(t)\frac{\partial C_{Mn(aq)}}{\partial z} + D(z,t)\frac{\partial^2 C_{Mn(aq)}}{\partial z^2} - \beta_{MnOx,Mn}V_{MnOx}X_{MnOx}\left(\frac{C_{DO}}{K_{DO}+C_{DO}}\right)\left(\frac{C_{Mn(aq)}}{K_{MnOx}+C_{Mn(aq)}}\right)$$
$$+\beta_{an,Mn}V_{an}X_{an}I\left(\frac{C_{DOC}}{K_{DOC}+C_{DOC}}\right) \tag{5}$$

$$\frac{\partial C_{DOC}}{\partial t} = -v(t)\frac{\partial C_{DOC}}{\partial z} + D(z,t)\frac{\partial^2 C_{DOC}}{\partial z^2} - \beta_{ar,DOC}V_{ar}X_{ar}\left(\frac{C_{DO}}{K_{DO}+C_{DO}}\right)\left(\frac{C_{DOC}}{K_{DOC}+C_{DOC}}\right)$$
$$-\beta_{an,DOC}V_{an}X_{an}I\left(\frac{C_{DOC}}{K_{DOC}+C_{DOC}}\right) \tag{6}$$

where $\beta_{ar,DO}$, $\beta_{MnOx,DO}$, $\beta_{MnOx,Mn}$, $\beta_{an,Mn}$, $\beta_{ar,DOC}$, and $\beta_{an,DOC}$ are stoichiometric coefficients, V_k is the maximum

microbial rate of the kth reaction, X_k is the microbial biomass facilitating the kth reaction, and K_j is the half saturation
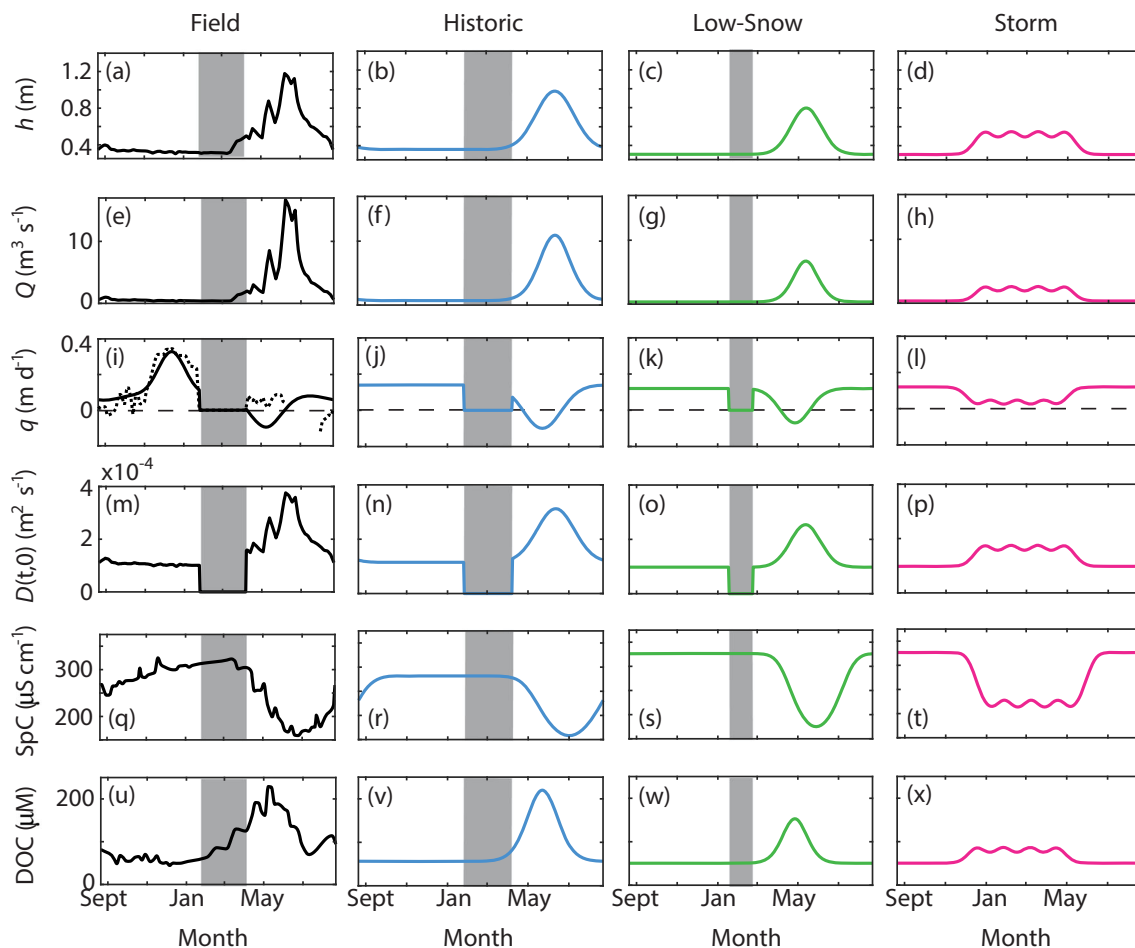
Fig. 4 Idealized inputs for the field model (first column) and three climate scenarios: 'historic' (second column), 'low-snow' (third column), and 'storm' (fourth column). Inputs include **a**–**d** stage (*h*), **e**–**h** river discharge (*Q*), **i**–**l** vertical Darcy velocity (*q*), **m**–**p** effective dispersion due to hyporheic mixing [*D*(*t*,0)], **q**–**t** specific conductance of river water (SpC), and **u**–**x** concentration of DOC in river water. The dotted line (**i**) represents estimates made in 1DTempPro for location B. Estimates differ from prescribed values in the field model due to efforts to fit observed conservative solute profiles. Shaded gray regions denote periods of streambed freezing

constant for the *j*th species (Table 2). Model reactions include aerobic respiration (denoted with subscript ar), Mn-oxide respiration (an), and $Mn_{(aq)}$ oxidation (MnOx; Fig. 1). Mn-oxides were assumed to be abundant and nonlimiting to the rate of Mn-oxide respiration. Inhibition (*I*) of Mn-oxide respiration in the presence of DO is represented as:

$$I = \frac{K_I}{K_I + DO} \qquad (7)$$

where K_I is the inhibition constant (Table 2).

Values of *v*(*t*) were guided by the results of heat tracing with one important difference: downwelling conditions were assigned to the rising limb of the spring snowmelt event, and upwelling conditions were assigned to the falling limb, despite heat tracing results that suggested more neutral to downwelling conditions (Fig. 4i, dashed line). These adjustments greatly improved the match with measured specific conductance profiles in May and July and were deemed reasonable for the following reasons:

temperature sensors were disturbed by the spring snowmelt event, leading to greater uncertainties in heat tracing during that interval, and heat tracing has been shown to be biased towards downwelling conditions (Irvine et al. 2015). In addition, the uppermost sensor at 10 cm is fairly shallow and is likely influenced by small-scale mixing in the shallow streambed promoted by dunes and ripples (Cardenas and Wilson 2007) and may not capture dominant groundwater upwelling (Cuthbert and MacKay 2013).

D(*t*,*z*) was assumed to be equal for all species: there is no mass-dependent partitioning of solutes (e.g. Knights et al. 2017; Zarnetske et al. 2012). *D*(*t*,*z*) includes the effects of pore-scale mechanical dispersion, as well as small-scale advective transport processes that occur in multiple dimensions within the hyporheic zone but have a predominantly vertically directed, dispersion-like effect on solute transport at shallow depths (Grant et al. 2012; O'Connor and Harvey 2008; Voermans et al. 2018). At the sediment–water interface (*z* = 0), *D* is dominated by effective dispersion due to small-scale

Table 2 Model parameters

Parameter	Description	Value (units)	Source
Physical parameters			
D_p	Mechanical dispersion at bottom boundary	1×10^{-7} (m^2 s^{-1})	Fitted
D_m	Molecular diffusion	1×10^{-10} (m^2 s^{-1})	Ingebritsen and Ward (1998)
G	Constant of decay for $D(t,z)$	41 (m^{-1})	Fitted
k	Permeability	2.42×10^{-9} (m^2)	Observed
n	Porosity	0.27	Observed
q_F	Darcy velocity during freezing	0 (m s^{-1})	–
S	Channel slope	0.008	Observed
v_k	Kinematic viscosity of freshwater	1.13×10^{-6} (m^2 s^{-1})	–
Reaction kinetics			
$\beta_{an,DOC}$	Stochiometric coefficient: DOC in anaerobic respiration	1	Stoichiometry
$\beta_{an,Mn}$	Stochiometric coefficient: Mn$_{(aq)}$ in anaerobic respiration	2	Stoichiometry
$\beta_{ar,DOC}$	Stochiometric coefficient: DOC in aerobic respiration	1	Stoichiometry
$\beta_{ar,DO}$	Stochiometric coefficient: DO in aerobic respiration	1	Stoichiometry
$\beta_{MnOx,Mn}$	Stochiometric coefficient: Mn$_{(aq)}$ in Mn oxidation	1	Stoichiometry
$\beta_{MnOx,DO}$	Stochiometric coefficient: DO in Mn oxidation	0.5	Stoichiometry
C	Constant of decay for microbial biomass	3 (m^{-1})	Fitted
K_{DOC}	Half saturation constant for DOC	0.5 (mM)	Gu et al. (2007); Knights et al. (2017); Sawyer (2015); Zarnetske et al. (2012)
K_I	Inhibition constant for Mn-oxide respiration	7.5 (µM)	Gu et al. (2007); Knights et al. (2017); Sawyer (2015); Zarnetske et al. (2012)
$K_{Mn,ox}$	Half saturation constant for Mn in Mn oxidation	0.6 (µM)	Tebo and Emerson (1986)
K_{DO}	Half saturation constant for DO	0.165 (mM)	Abrams and Loague (2000); Gu et al. (2007); Knights et al. (2017); Rifai and Bedient (1990); Sawyer (2015); Zarnetske et al. (2012)
V_{an}	Maximum microbial rate of Mn-oxide respiration	0.7 (h^{-1})	Abrams and Loague (2000); Gu et al. (2007)
V_{ar}	Maximum microbial rate of aerobic respiration	1 (h^{-1})	Gu et al. (2007); Guillemette and Giorgio (2011); Knights et al. (2017); Zarnetske et al. (2012)
V_{MnOx}	Maximum microbial rate of Mn oxidation	0.1 (h^{-1})	Harvey and Fuller (1998); Shiller and Stephens (2005)
$X_{an,GW}$	Biomass of Mn-oxide respirers in groundwater	1 (µM)	Hendricks (1996); Marmonier et al. (1995); Schallenberg and Kalff (1993)
$X_{an,RW}$	Biomass of Mn-oxide respirers in river water	0.15 (mM)	Holmes et al. (2012a); Li et al. (2010); Pallud and Van Cappellen (2006)
$X_{ar,GW}$	Biomass of aerobes in groundwater	10 (µM)	Hendricks (1996); Marmonier et al. (1995); Schallenberg and Kalff (1993)
$X_{ar,RW}$	Biomass of aerobes in river water	1.5 (mM)	Battin et al. (2003); Battin et al. (2016); Lock et al. (1984); Mendoza-Lera et al. (2017)
$X_{MnOx,GW}$	Biomass of Mn oxidizers in groundwater	1 (µM)	Hendricks (1996); Marmonier et al. (1995); Schallenberg and Kalff (1993)
$X_{MnOx,RW}$	Biomass of Mn oxidizers in river water	0.15 (mM)	Emerson and Moyer (1997)
River-water concentrations			
$C_{Mn(aq),RW}$	Concentration of Mn$_{(aq)}$	9 (nM)	Observed
$C_{DO,RW}$	Concentration of DO	0.25 (mM)	Observed
Groundwater concentrations			
$C_{DOC,GW}$	Concentration of DOC	0.5 (µM)	–
$C_{Mn(aq),GW}$	Concentration of Mn$_{(aq)}$	23 (µM)	Observed
$C_{DO,GW}$	Concentration of DO	25 (µM)	Observed
$C_{SpC,GW}$	Specific conductance	500 (µS cm^{-1})	Observed

hyporheic mixing, which varies seasonally with bed shear stresses according to Eq. 13 of Voermans et al. (2018):

$$D(t,0) = 1.9\text{Re}_K(t)^2\text{Sc}(t)D_m \quad (8)$$

$$\text{Sc}(t) = \frac{v_k}{D_m} \quad (9)$$

$$\text{Re}_K(t) = \frac{\sqrt{k}u^*(t)}{v_k} \quad (10)$$

where $\text{Re}_K(t)$ is the Permeability Reynold's number, $\text{Sc}(t)$ is the Schmidt number, D_m is molecular diffusion (Table 2), v_k is kinematic viscosity of freshwater (Table 2), k is permeability (Table 2), and u^* is shear velocity:

$$u^*(t) = \sqrt{gh(t)S} \quad (11)$$

where g is gravitational force, $h(t)$ is stage height (Fig. 4), and S is channel slope (Table 2). Permeability was estimated from a constant head permeameter test using a Darcy tube (Gilson Company, Inc., OH, USA) packed with sediment collected from location B. Five flow rates were measured using five unique head differences, and permeability was determined based on Darcy's Law. Kinematic viscosity (v_k) was assumed to be invariant with temperature.

$D(t,z)$ was assumed to decline exponentially as the rate of small-scale hyporheic advection declines (Elliott and Brooks 1997) and converge on a value representative of pore-scale mechanical dispersion ($D_p = 1 \times 10^{-7}$ m^2 s^{-1}) at the base of the model (Table 2). Specifically:

$$D(t,z) = \left[D(t,0) - D_p\right]\exp(Gz) + D_p \quad (12)$$

Facultative microbial biomass in the bed of East River has not been quantified, but inferences from Chafiq et al. (1999), Hou et al. (2017), and Van Gestel et al. (1992) suggest there are more microbes in near-surface hyporheic zones due to increased hyporheic exchange and supply of DOC and DO. It was assumed that biomass declines exponentially with depth by approximately two orders of magnitude:

$$X_k(t,z) = \left(X_{k,RW} - X_{k,GW}\right)\exp(Cz) + X_{k,GW} \quad (13)$$

where k denotes aerobes (ar), Mn-oxide respirers (an), and Mn$_{(aq)}$ oxidizers (MnOx). $X_{k,RW}$ and $X_{k,GW}$ are microbial biomasses in river water and groundwater, respectively (Table 2).

To solve Eqs. (3)–(6), boundary conditions were assigned based on measured concentrations in river water and deepest pore water. River-water concentrations varied with season (Fig. 4), while groundwater concentrations at the lower boundary were held constant (Table 2). Reaction kinetics were guided by the literature (Table 2) and refined to achieve the best visual fit with measured reactive solute concentrations (DO and Mn$_{(aq)}$). When the streambed was presumed frozen (see section 'Estimating seepage fluxes using temperature time series'), advection and reactions were halted, and the coefficient of dispersion was set to a constant equal to molecular diffusion in ice (Table 2). The transport equations were solved using COMSOL (COMSOL, Inc., Burlington, MA, USA), a generic finite element solver. Grid sensitivity analysis was performed and a mesh size no greater than 0.1 cm over the 1-m domain was chosen. The model reached steady annual cycles after 1 year of spin-up, so model results are reported from simulation year two. All model parameter values and descriptions, along with supporting literature, are summarized in Table 2. A sensitivity analysis with four of the less constrained model parameters is also included in the ESM.

Model case studies

To understand the effect of changes in hydrology on Mn cycling in the bed of the East River, three scenarios were simulated: historic, low-snow, and storm (Fig. 4). The historic scenario (Fig. 4, second column) reflects conditions similar to those captured during field measurements, with a long winter freezing period and a large annual snowmelt event (Fig. 3). The low-snow (Fig. 4, third column) scenario has a freezing period that is half the duration of the historic scenario. The annual discharge is decreased by 50% with respect to the historic scenario, corresponding with the upper limit for the predicted change in annual discharge of Colorado alpine streams by the mid-2000s (Vano et al. 2012). Additionally, the annual snowmelt event occurs one month earlier in the year and is smaller in magnitude and duration (Fig. 4c). In the storm scenario (Fig. 4, fourth column), the annual discharge is still decreased by 50% with respect to the historic scenario, but event flow is distributed across multiple storms in late winter through early spring instead of a large snowmelt pulse, and the streambed does not freeze (Fig. 4d). These three simulations represent a wide range of end-members that bound plausible hydrograph scenarios for the Rocky Mountains (Pederson et al. 2011; Rood et al. 2008; Stewart 2009).

In each of the three scenarios, idealized functions were chosen to represent the following time-dependent parameters: stage height [$h(t)$], stream discharge [$Q(t)$], vertical Darcy velocity [$q(t)$], effective dispersion [$D(t,0)$], specific conductance in the river [$C_{SpC,RW}(t)$], and DOC in the river [$C_{DOC,RW}(t)$] (Fig. 4). Stage and discharge were related through a rating curve (ESM). Darcy velocity, stream water conductance, and stream DOC concentration were linked to changes in stage height and discharge (ESM). $D(t,0)$ was calculated using Eqs. (8)–(11).

Results

Observations of vertical flow and geochemical transport are presented and used to test a reactive Mn transport model. The

effects of three unique hydrograph scenarios on Mn transport in the streambed are then presented.

Seasonal changes in river-water/groundwater interactions

Upwelling conditions dominated at the three locations over much of the year, particularly during the baseflow months (mid-August until time of freezing; Fig. 5). A switch to downwelling conditions generally occurred when stream discharge increased in the spring. Location A experienced the longest downwelling conditions from the time of thaw in April 2017 until monitoring ceased in August 2017. Location C appears to have experienced a similar period of downwelling conditions, but there was a gap in the record during flood conditions due to sensor dislodgement. At location B, downwelling initiated later in the spring snowmelt season, likely around the time of peak discharge in June. The magnitude of downwelling was also less at location B than A and C. Location B had the greatest rate of peak

groundwater discharge (0.33 ± 0.026 m day^{-1}) and greatest average groundwater discharge over the year (0.11 ± 0.026 m day^{-1}).

Location B was frozen for only 2 months, while location A was frozen for more than four months (Fig. 5). All locations thawed within 1 week of one another, but freeze up occurred in early December at A, late December at C, and late January at B. These observations are consistent with the stronger rate of upwelling at B, which should buffer wintertime temperatures. Taken together, location A is interpreted to be more river-water influenced, while locations B and C are more groundwater influenced.

Seasonal changes in pore-water chemistry

Specific conductance generally increased with depth below the sediment–water interface (Fig. 6, left column). At location A, relatively small and stable vertical gradients indicate deep mixing of low-conductivity river water across seasons. At location B, steeper gradients indicate upwelling of high-conductivity groundwater over most of the year. During the rising hydrograph in May, however, river water mixed deep in the bed. At location C, specific conductance values were generally intermediate between locations A and B. For all locations, conductance was notably lower in May and July, compared to August and October, due to mixing of low-conductivity river water deeper in the streambed during the snowmelt event (Fig. 6, left column).

Strontium-87 to Strontium-86 (^{87}Sr/^{86}Sr) ratios have been used as a tracer to understand hyporheic flow paths (Lyons et al. 1995; Palmer and Edmond 1989; Stewart et al. 1998; Fig. 6, second column). Location B had consistently higher ratios that may reflect groundwater influence or longer residence times, while A and C had a wider range of values that may reflect a greater portion of river-derived (hyporheic) waters with a range of residence times. Notably, August and October ratios for location C were similar to those of B, indicating older groundwater influence during the baseflow season.

DO concentrations generally decreased with depth below the sediment–water interface (Fig. 6, third column), as expected due to aerobic respiration and $Mn_{(aq)}$ oxidation (Boano et al. 2010; Lensing et al. 1994; Zarnetske et al. 2012). For most locations and months, a decline occurred at about a 20–30 cm depth. DO penetrated deepest at all locations during May (B) or July (A and C) when river discharge was high (Fig. 6, third column). DOC concentrations were not measured due to limited sample volume, but Nelson et al. (2019) found pore-water concentrations ranged from <0.031 (detection limit) to 0.26 mM and averaged 0.070 mM within the study reach.

$Mn_{(aq)}$ concentrations at location A were low (<7.5 µM) compared to locations B and C (Fig. 6, fourth column). At
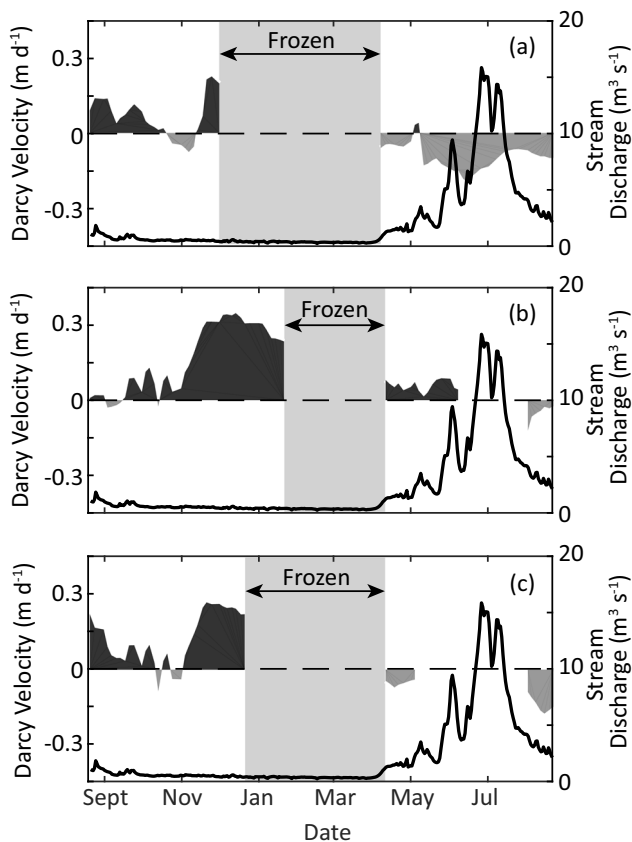
Fig. 5 Rates of vertical Darcy velocity (q) at locations **a** A, **b** B, and **c** C (Fig. 2). Stream discharge (solid black line) is shown as a reference. Positive values indicate upwelling (shaded black), while negative values indicate downwelling (shaded dark grey). Error for estimates is ±0.026 m day^{-1} (as presented in the ESM). Periods without q estimates during the snowmelt event are due to sensor disturbance. Discharge was obtained from Carroll and Williams (2019)

Fig. 6 Depth profiles for SpC (first column), $^{87}Sr/^{86}Sr$ (second column), DO (third column), and $Mn_{(aq)}$ (fourth column) at locations **a**–**d** A, **e**–**h** B, and **i**–**l** C (data available in Saup et al. 2019). $Mn_{(aq)}$ values lower than the detection limit are reported as the detection limit (Bryant 2019). Samples in May at location A were collected in a slightly offset location due to safety consider- ations with wading in high water, which may explain the seemingly groundwater-influenced profiles of higher SpC and lower DO
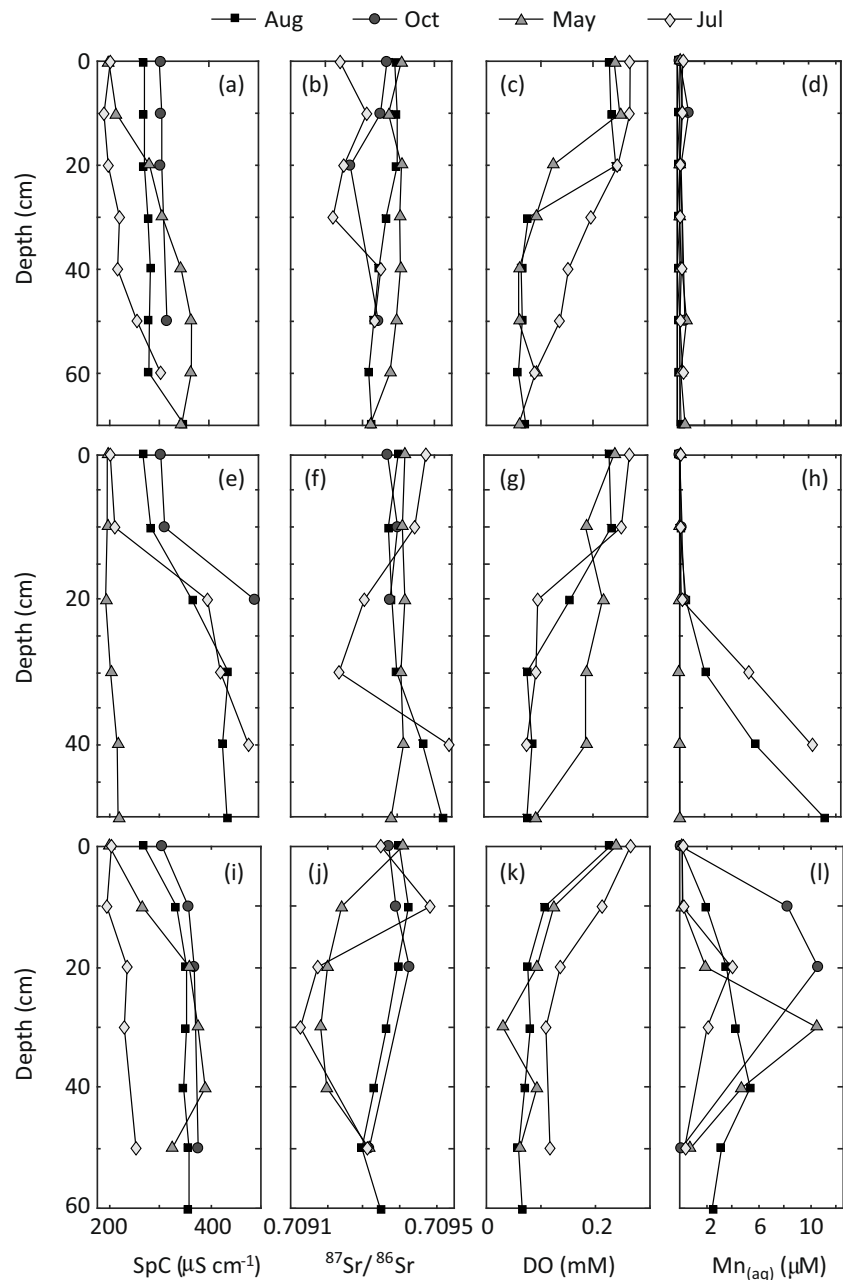
location B, $Mn_{(aq)}$ was only low in May, when DO penetrated deeper in sediments during the flood stage. In July and August, discharging groundwater carried $Mn_{(aq)}$ toward the sediment–water interface, and $Mn_{(aq)}$ concentrations increased below 20 cm (Fig. 6, fourth column). A sea- sonal shift in the $Mn_{(aq)}$ profile was also evident at location C: the peak $Mn_{(aq)}$ concentration shifted up- ward from 30 cm in May to 20 cm in October, towards the end of the baseflow season (Fig. 6l). In general, $Mn_{(aq)}$ concentrations were low when DO was high and increased with specific conductance, used here as a proxy for groundwater influence (Fig. 7a). For com- parison, dissolved chromium exhibited an opposite

relationship with DO, as the soluble form is the oxi- dized form, unlike Mn (Fig. 7b). Values of pH varied over a small range, generally between 7.5 and 8.5 (Fig. S1 of the ESM).

Trace metals such as zinc, lead, and copper tended to have lower concentrations in the baseflow season (~0.05–0.06 μM) that increased during spring snowmelt (May and July) in both river water and pore water (up to 0.4 μM; Fig. S1 of the ESM). Copper had the highest concentrations of the three metals (up to 0.4 μM), while lead had significantly lower concentrations for all months, depths, and locations (up to 0.03 μM). Because concentrations tended to increase in both river water and deep pore water during the hydrograph peak, both river water and
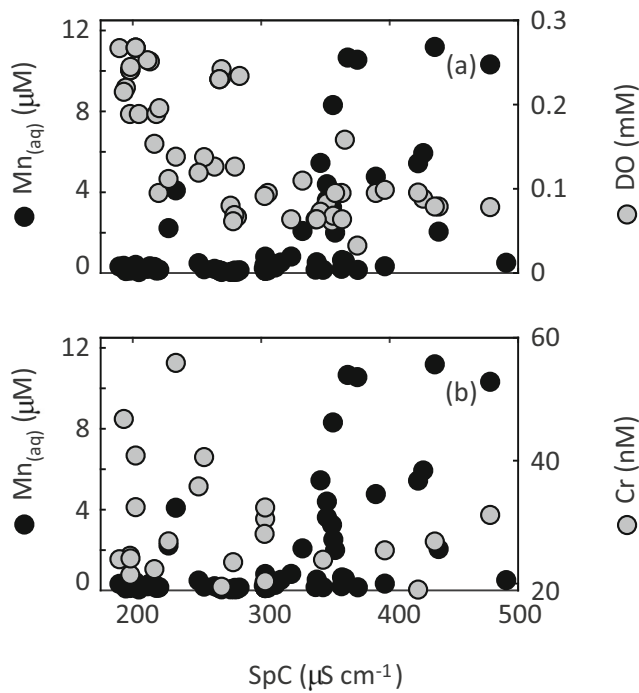
Fig. 7 $Mn_{(aq)}$ compared to **a** DO, and **b** chromium (Cr) for all locations (A, B, and C) and seasons (August, October, May, and July) along a mixing line between river water (low SpC) and groundwater (high SpC; Saup et al. 2019). $Mn_{(aq)}$ values lower than the detection limit are reported as the detection limit (Bryant 2019)

groundwater may serve as metal sources to the hyporheic zone. Copper concentrations were generally lower between 10 to 30 cm below the sediment–water interface, suggesting potential immobilization in shallow sediments, perhaps on Mn-oxides (Fuller and Harvey 2000; Kay et al. 2001; Schäffner et al. 2015; Fig. S1 of the ESM).

Model comparison with field measurements

Location B was identified as an ideal site for model development because it was well represented by 1D

transport. Location A was not simulated because concentrations of $Mn_{(aq)}$ remained low over all sampled depths and seasons. At location C, concentrations peaked at an intermediate depth, suggesting the possibility of multiple geochemical end members or horizontally stratified flows that are not well captured by a 1D vertical model. A gravel layer mapped by Malenda (2018) may promote horizontal flow near location C.

All modeled specific conductance profiles at location B were in good agreement with measurements (Fig. 8a). Specific conductance decreased in May as stream water intruded during the rising limb of the spring snowmelt event, then increased in association with groundwater upwelling (Fig. 8a). The model also captured the increase in DO and decrease in $Mn_{(aq)}$ in May during downwelling conditions (Fig. 8b). Although modeled DO concentrations decayed faster with depth than observations (especially in May), the sampling technique exposed samples to DO from the atmosphere, and it was estimated that the practical detection limit of this method was 0.0625 mM. The model accurately characterized shifts in the $Mn_{(aq)}$ concentration profile over July and August (Fig. 8c). Sensitivity of the simulated profiles to a collection of less constrained input parameters is presented in the ESM.

Model hydrograph scenarios

Under the historic scenario, or idealized present day conditions, low-conductivity river water mixes deep into the streambed over the rising limb of the spring snowmelt (April through mid-May; Fig. 9d). DO penetrates deep (>50 cm) into the streambed (Fig. 9g), while $Mn_{(aq)}$ concentrations decline abruptly (Fig. 9m). This decline is primarily driven by the advective transport of low-$Mn_{(aq)}$, low-specific conductance river water down through the profile. The result is a decline in the $Mn_{(aq)}$ oxidation rate, calculated as the magnitude of the

Fig. 8 Comparison between measured (solid points) and modeled (solid lines) results for **a** SpC, **b** DO, and **c** $Mn_{(aq)}$ using the field model at location B for August, October, May, and July
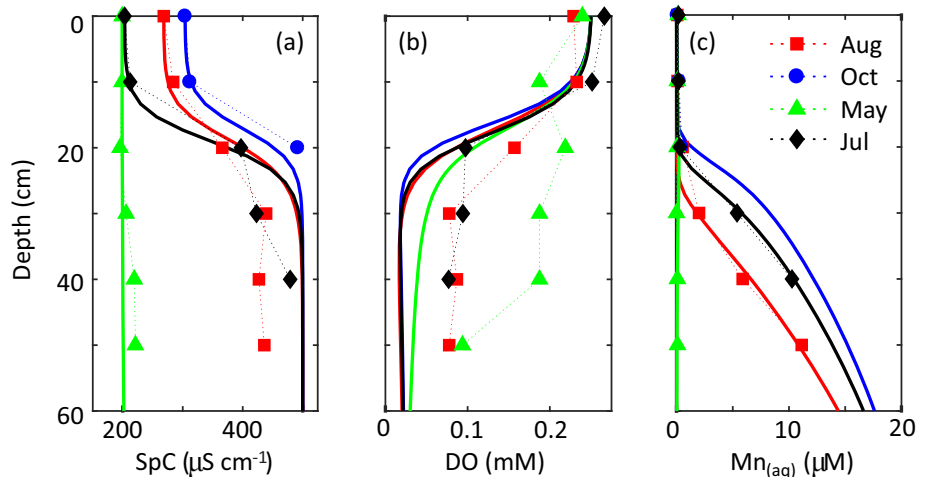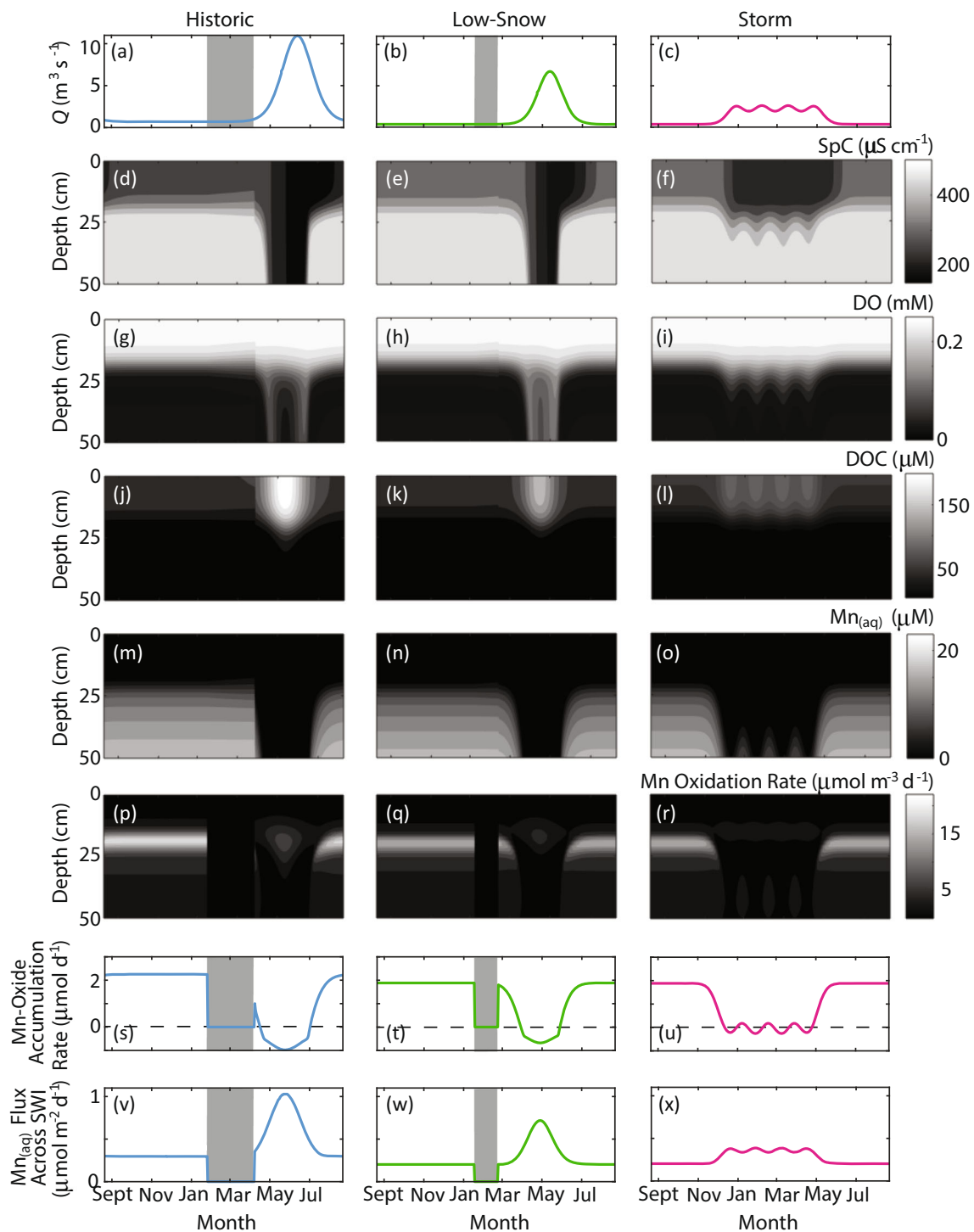
Fig. 9 Model results for three climate scenarios: historic (left column), low-snow (middle column), and storm (right column). Stream discharge (Q) (**a–c**) for the three scenarios is shown for comparison. Results are shown over a 1-year period from 21 August to 21 August of the following year, and include **d–f** SpC, **g–i** DO, **j–l** DOC, **m-o** Mn$_{(aq)}$, **p–r** Mn oxidation rate, **s–u** Mn-oxide accumulation rate, and **v-x** Mn$_{(aq)}$ flux across the sediment–water interface (SWI). Models were allowed a 1-year spin-up period

third term on the right side of Eq. (5) (Fig. 9p). In May, as DOC concentrations increase in the upper 25 cm of the streambed (Fig. 9j), aerobic respiration restricts the depth of DO penetration (Fig. 9g). Rates of Mn-oxide respiration also increase slightly with the enhanced supply of DOC, leading to

a small region of elevated Mn$_{(aq)}$ (<0.3 μM) near 20 cm. This subtle increase in Mn$_{(aq)}$ concentrations allows for a small region where Mn-oxides form between 15 and 25 cm (Fig. 9p). In mid-May through mid-June, declining DOC concentrations (Fig. 9j) limit aerobic and anaerobic respiration,

leading to a brief increase in DO between 20 and 50 cm (Fig. 9g). Rates of Mn oxidation (Fig. 9p) remain low due to a limited supply of $Mn_{(aq)}$ from groundwater. Over the recession and baseflow season (mid-June through Feb), river water penetrates less deeply to about 20 cm (Fig. 9d), and upwelling groundwater supplies $Mn_{(aq)}$ to shallower pore water below 20 cm (Fig. 9m). DO and DOC only mix to depths of approximately 20 and 15 cm, respectively (Fig. 9g, j). As upwelling groundwater transports $Mn_{(aq)}$ up through the streambed profile (Fig. 9m), Mn oxidation rates increase, peaking between 15 and 25 cm (Fig. 9p). Above 15 cm, rates of Mn oxidation are low, despite high DO concentrations (Fig. 9g), because the supply of $Mn_{(aq)}$ from groundwater has been exhausted by deeper oxidation, and river water contributes little to the $Mn_{(aq)}$ supply (Fig. 9m). During frozen conditions, solute concentrations remain nearly steady as a result of negligible transport and reactions.

The accumulation rate of Mn-oxides beneath a unit area of streambed was calculated as the integral with depth of the difference between Mn oxidation and Mn-oxide respiration over the upper 50 cm of the streambed. Positive values indicate more oxidation than Mn-oxide respiration, or net sequestration of Mn as Mn-oxides (Fig. 9s). Over the rising limb of the spring snowmelt, $Mn_{(aq)}$ is released (net Mn-oxide respiration occurs) because oxidation is limited by the supply of $Mn_{(aq)}$ from groundwater, and Mn-oxide respiration is enhanced by the supply of DOC from river water. The maximum rate of Mn mobilization is -0.98 μmol day^{-1} (Fig. 9s). Mn-oxides then accumulate over the falling limb of the hydrograph as Mn-oxide respiration becomes limited by declining DOC concentrations and Mn oxidation is enhanced by an increase in $Mn_{(aq)}$ supply from groundwater. The maximum accumulation rate of 2.26 μmol day^{-1} is maintained over most of the baseflow season. The yearly average Mn-oxide accumulation rate is 1.06 μmol day^{-1}.

$Mn_{(aq)}$ flux, calculated as the integral of the total flux of $Mn_{(aq)}$ across the sediment–water interface, is always positive, or directed from the aquifer to the stream (Fig. 9v), despite low $Mn_{(aq)}$ concentrations in the upper 15 cm of streambed. During spring, the downward-directed advective flux is compensated for by an increase in dispersive flux. This increase in dispersive flux occurs due to a combination of increased shear stress at the sediment–water interface (Eqs. 8–11) and a slight increase in $Mn_{(aq)}$ concentrations in the upper streambed resulting from an increase in DOC concentrations (Fig. 9j) enhancing Mn-oxide respiration. A maximum flux of 1.03 μmol m^{-2} day^{-1} occurs in late May. Over the recession and baseflow period, the flux decreases to 0.30 μmol m^{-2} day^{-1} as dispersion due to hyporheic mixing and the supply of DOC for Mn-oxide respiration decrease. Assuming a homogeneous channel with an average width of 8.5 m, the

average flux to the river per linear km of channel is 2.96 mmol day^{-1}. It is important to note that these fluxes to the stream are very small. For comparison, the downstream flux of $Mn_{(aq)}$ in the river during baseflow is ~1,400 mmol day^{-1} at the Pumphouse.

In the low-snow scenario with a smaller spring snowmelt event and shorter freezing period, baseflow conditions persist for a greater portion of the year, about 9 months instead of 7 (Fig. 9e). During spring snowmelt, DOC from river water is restricted to shallower depths of 20 cm (Fig. 9k) compared to 25 cm for the Historic scenario, leading to a shorter period of net Mn-oxide respiration in April and a less negative rate of Mn-oxide accumulation (-0.68 μmol day^{-1} versus -0.98 μmol day^{-1}; Fig. 9t). During baseflow, Mn-oxide accumulation rates are lower compared to the Historic scenario (1.88 μmol day^{-1} versus 2.26 μmol day^{-1}; Fig. 9t) due to a lower rate of groundwater upwelling, which supplies $Mn_{(aq)}$ for oxidation (Fig. 9n). Averaged over the year, the Mn-oxide accumulation rate is slightly greater than the historic scenario (1.18 μmol day^{-1} versus 1.06 μmol day^{-1}) as the result of two effects: (1) a prolonged (but weaker) upwelling period that promotes Mn oxidation for a greater portion of the year (Fig. 9q), and (2) a smaller pulse of DOC into the streambed during spring snowmelt (Fig. 9k), which limits Mn-oxide respiration.

$Mn_{(aq)}$ fluxes across the sediment–water interface in the low-snow scenario are significantly lower during peak downwelling conditions compared to the historic scenario (0.72 μmol day^{-1} m^{-2} versus 1.03 μmol day^{-1} m^{-2}) due to a decrease in dispersive mixing and DOC penetration (Fig. 9w). Fluxes are also lower during baseflow compared to the Historic scenario (0.20 μmol day^{-1} m^{-2} versus 0.30 μmol day^{-1} m^{-2}) due to a decrease in advective flux associated with less groundwater upwelling (Fig. 9w). It is important to note that lower stage height during baseflow in a low-snow year is assumed to result in lower rates of groundwater upwelling (ESM). This relationship may not occur in all alpine river reaches and is hard to predict given complex interactions between climate, vegetation, and recharge. Averaged over the entire year, the flux to the river per linear km is less than the historic scenario (2.12 mmol day^{-1} versus 2.96 mmol day^{-1}).

In the storm scenario with distributed, small precipitation events, baseflow conditions span only half the year. The depth of river-water mixing is more constant over the year and is limited to ~35 cm during storm events (Fig. 9f). With each storm, $Mn_{(aq)}$ concentrations in the upper 50 cm of the streambed decline (Fig. 9o), leading to a decline in rates of Mn oxidation (Fig. 9r). Because DOC only penetrates to depths of ~20 cm, during storm events (Fig. 9l), rates of Mn-oxide respiration remain limited. Only brief periods of net Mn-oxide respiration occur (Mn-oxide accumulation rate of -0.26 μmol day^{-1}; Fig. 9u). Over the baseflow season, the Mn-oxide accumulation rate is the same as the low-snow scenario

(1.88 µmol day^{-1}) because rates of groundwater upwelling and hyporheic mixing remain unchanged (Fig. 9u). Since the baseflow season is shorter than either the low-snow or historic scenarios, the annual average Mn-oxide accumulation rate is lower (1.04 µmol day^{-1}).

The flux of Mn$_{(aq)}$ to the river is more constant in the storm scenario, with multiple small fluctuations (Fig. 9x) instead of one large pulse. Peak Mn$_{(aq)}$ fluxes associated with storms are significantly less than peak fluxes associated with snowmelt. These peaks are largely driven by the increase in DOC supply to shallow sediments (Fig. 9l). During baseflow, the flux of Mn$_{(aq)}$ across the sediment–water interface is 0.20 µmol day^{-1} m^{-2} (the same as the low-snow scenario; Fig. 9x). The yearly Mn$_{(aq)}$ flux to the river per km is 2.29 mmol day^{-1}, which is greater than the low-snow scenario because a long storm season with multiple small pulses of Mn$_{(aq)}$ leads to a greater annual flux than one large snowmelt event. Additionally, the streambed never freezes, so fluxes never cease entirely (Fig. 9x).

Discussion

Under current "typical" hydrograph conditions, East River, Colorado experiences large seasonal shifts in river-water/groundwater mixing that lead to predictable seasonal changes in Mn$_{(aq)}$ flux and Mn-oxide formation, but the dynamics differ from observations from mining-impacted streams. In the more pristine East River where discharging groundwater is the main source of Mn$_{(aq)}$, rates of Mn-oxide formation are greatest in the summer and fall baseflow season, zero in frozen winter conditions, and negative in spring snowmelt, when a greater DOC supply to the hyporheic zone drives a shift to net Mn-oxide respiration and mobilization. Fluxes of Mn$_{(aq)}$ to the river are moderate during the baseflow season, zero in frozen winter conditions, and greatest during spring snowmelt resulting from significant hyporheic mixing and an increase in DOC supply for Mn-oxide microbial respiration. In contrast, Robbins and Corley (2005) observed increases in the concentration of Mn-oxides in spring and summer months in the hyporheic zone of an alpine stream in Arizona, rather than summer and fall. Similar to Robbins and Corley (2005), August et al. (2002) demonstrated that an alpine wetland impacted by acid mine drainage functioned as a net sink of Mn during spring snowmelt, while the East River streambed appears to be a source. In these prior studies, Mn$_{(aq)}$ concentrations in river water ranged up to 1 mM. At East River, river-water concentrations are generally ~1 µM, and the main source of Mn$_{(aq)}$ to the hyporheic zone is groundwater. Spring snowmelt results in downwelling river water, which limits the supply of Mn$_{(aq)}$ and enhances the supply of DOC, leading to Mn-oxide respiration. During baseflow conditions,

however, geochemically reduced groundwater supplies Mn$_{(aq)}$ to the oxygenated, shallow streambed, and Mn oxidation rates are greatest.

In pristine streambeds like that of the East River, a shift towards a longer baseflow period under a warmer climate should result in greater accumulation of Mn-oxides in the shallow streambed and sequestration of metals that sorb to them. In model scenarios shown here, a later, smaller snowmelt event indeed favors slightly greater annual average rates of Mn-oxide accumulation in the upper 50 cm of the streambed, potentially by ~10 for a 50% decrease in annual stream discharge (low-snow scenario). This 10% change is sensitive to the rate of groundwater discharge during the baseflow season, since groundwater supplies Mn for microbial oxidation. The rate of groundwater discharge during the baseflow season is assumed to decline (by 15%) in drier years (ESM) in the idealized scenarios, but the exact magnitude of the change in natural alpine reaches is difficult to predict because it depends on basin-scale flow paths that are influenced by local geology and vegetation. If groundwater discharge to the stream during the baseflow season is more drastically reduced, the annual average rate of Mn-oxide accumulation will decrease, despite the longer duration of the baseflow season. Under the storm-dominated hydrological regime with the same 50% decline in annual stream discharge but a shorter baseflow season, average rates of Mn-oxide accumulation decrease by ~2% instead of increasing, and the dynamics are very different due to the lack of a large Mn mobilization event associated with a spring snowmelt pulse. Both warmer, drier scenarios lead to declines in the export of Mn$_{(aq)}$ to pristine alpine rivers. In the low-snow scenario, the yearly Mn$_{(aq)}$ flux from the aquifer to the river decreases by ~30% compared to the historic scenario in response to a smaller snowmelt event. Under the storm scenario, the Mn$_{(aq)}$ flux to the river decreases by ~20%, primarily due to the lack of a large snowmelt flux. These scenarios show the combined importance of the duration of baseflow, event flows, and frozen bed conditions for Mn fate in pristine mountain streams.

The idealized model scenarios presented here do not replace the need for monitoring metal export and retention in alpine streams, which are subject to heterogeneous and complex hydrologic and biogeochemical processes that were necessarily simplified in the models presented in this study—for example, the microbial communities were assumed to remain steady in all scenarios. These communities are likely to respond to a changing hydrograph. Danczak et al. (2016) show that microbial communities in the hyporheic zone of the Colorado River change seasonally, which could result in changes in Mn processing (Clements et al. 2008). Microbial communities and activities can also be affected by changes in temperature, which were not incorporated in these models (Kaplan and Bott 1989; Storey

and Williams 2004); however, Battin (2000) showed that hyporheic microbial activity was not well correlated with temperature over an annual range similar to that of the East River. Unexpected changes in the quality or quantity of DOC in stream water were also not accounted for, which may occur in a changing climate (Harte et al. 2015; Mann et al. 2012; O'Donnell et al. 2010). Such changes would impact Mn transport but are outside the scope of this study and should be assessed in future work. The assumption was made that DOC is limiting in groundwater, and organic matter as a source of DOC in the hyporheic zone was not included (Knights et al. 2017; Zarnetske et al. 2012). Given the significant pulse of DOC in the river water during spring snowmelt and the coarse nature of streambed gravels, sediment sources of DOC are unlikely to play a major role in alleviating DOC limitations on Mn-oxide respiration. It is possible that groundwater contains Mancos Shale-derived DOC, but many studies have shown such groundwater DOC to be less labile than terrestrially derived DOC in river water (Grøn et al. 1992; Schindler and Krabbenhoft 1998; Sobczak and Findlay 2002).

This study took a 1D approach to represent hyporheic transport. As such, these models did not explicitly incorporate multidimensional flow paths—for example, bedforms have been shown to promote downwelling conditions that deliver more oxygen to streambed sediments on the leeward side (Elliott and Brooks 1997; Shen et al. 1990), resulting in horizontal gradients in aerobic respiration and nitrate removal (Boano et al. 2010; Harvey and Bencala 1993). However, the overall effect of such small-scale features on vertical solute transport is captured in the effective dispersion coefficient (O'Connor and Harvey 2008; Voermans et al. 2018). This enhanced hyporheic mixing is vital to the Mn transport dynamics that were observed and modeled, because it facilitates the enhanced transfer of DO and DOC to shallow sediments, even when ambient groundwater is upwelling during baseflow conditions. If this mixing were absent (for example, as a result of even stronger ambient groundwater discharge or smaller bedform-current interactions), Mn oxides would form at the sediment–water interface or in the river-water column rather than beneath the sediment–water interface. In addition to the effects of small-scale multidimensional flow paths, lateral hyporheic flow paths at the scale of meanders connect recharge zones on the upslope edge of the meander with discharge zones on the opposite side of the bend (Boano et al. 2010). Such large-scale flow paths will likely have a predictable effect on Mn transport and transformation at the reach scale. Dwivedi et al. (2018) modeled lateral hyporheic flow through a meander of the East River directly downstream from this study site. They demonstrate that groundwater flow

through the floodplain traverses redox zones in which more energetically favorable TEAs such as DO are depleted and progressively less energetically favorable TEAs such as Fe and Mn are utilized. Lateral flow paths may explain some of the differences in vertical advective flux and deeper hyporheic pore-water chemistry between locations A and C, supported by findings of Nelson et al. (2019). Future field observations and streambed mapping could support the development of multidimensional hyporheic transport models to explore heterogeneity in Mn transport.

Mn-oxide concentrations or mineral composition were not measured, which would have required destructive sampling of the monitoring sites. Measuring changes in Mn-oxide concentrations and composition over seasons is an important area for future study. Furthermore, these models do not capture multiphase transport during frozen conditions (Kalousová et al. 2014). No sampling campaigns were conducted during winter due to difficultly extracting samples from the frozen subsurface. Winter is a time, however, when microbial activity (Liang et al. 2003; Zelles et al. 1991) and fluxes (Cherkauer and Lettenmaier 1999) are likely minimal.

Conclusion

The timing and magnitude of snowmelt events in pristine alpine river systems has a large impact on Mn transformation and mobility that differs from mining-impacted river systems, where $Mn_{(aq)}$ concentrations in river water can be much greater. During baseflow conditions when groundwater delivers $Mn_{(aq)}$ to the hyporheic zone, Mn oxidation occurs at shallow depths. A reversal to downwelling conditions during spring snowmelt results in a decrease in pore-water concentrations of $Mn_{(aq)}$ and an increase in DOC, simultaneously restricting Mn oxidation and enhancing Mn-oxide respiration. In years with less snowmelt, a diminished supply of DOC in spring should limit Mn-oxide respiration, and a longer baseflow season should increase the supply of $Mn_{(aq)}$ from groundwater for Mn-oxide formation. The net result of greater Mn-oxide accumulation should be to create additional sorption sites for other trace metals that influence water quality in mountain streams. In the absence of a frozen bed and large snowmelt event, a more subdued annual hydrograph is expected to result in smaller annual disturbances to Mn transport. These findings suggest that pristine systems such as the East River may prove more resilient to contaminant metal fluxes as a result of an accumulation of Mn-oxides, in contrast to mining-impacted sites that show different seasonal behaviors. It is therefore important to understand the sourcing of $Mn_{(aq)}$ in riverine systems because there

are important implications for water quality and stream health.

While many hyporheic modeling studies have focused on carbon and nitrate, models of dynamic Mn transport in hyporheic zones are limited. These models, developed from field observations of a pristine river, show that dynamic hyporheic mixing has large effects on Mn fate in streambeds. Future research should focus on two- and three-dimensional observations and models to understand the role that lateral flow plays in Mn transport and transformation. As climate changes and anthropogenic metal contamination in riverine systems intensifies, it will be imperative to understand the fate of Mn in alpine rivers and their sediments to better predict changes in metal mobility and water quality.

References

Abrams RH, Loague K (2000) A compartmentalized solute transport model for redox zones in contaminated aquifers: 1. theory and development. Water Resour Res 36(8):2001–2013. https://doi.org/10.1029/2000WR900110

August EE, Mcknight DM, Hrncir DC, Garhart KS (2002) Seasonal variability of metals transport through a wetland impacted by mine drainage in the Rocky Mountains. Environ Sci Technol 36(17):3779–3786. https://doi.org/10.1021/es015629w

Baalousha M, Stoll S, Motelica-Heino M, Guigues N, Braibant G, Huneau F, Le Coustumer P (2018) Suspended particulate matter determines physical speciation of Fe, Mn, and trace metals in surface waters of Loire watershed. Environ Sci Pollut Res 26:5251–5266. https://doi.org/10.1007/s11356-018-1416-5

Baker MA, Dahm CN, Valett HM (1999) Acetate retention and metabolism in the hyporheic zone of a mountain stream. Limnol Oceanogr 44(6):1530–1539. https://doi.org/10.4319/lo.1999.44.6.1530

Battin TJ (1999) Hydrologic flow paths control dissolved organic carbon fluxes and metabolism in an alpine stream hyporheic zone. Water Resour Res 35(10):3159–3169. https://doi.org/10.1029/1999WR900144

Battin TJ (2000) Hydrodynamics is a major determinant of streambed biofilm activity: from the sediment to the reach scale. Limnol Oceanogr 45(6):1308–1319. https://doi.org/10.4319/lo.2000.45.6.1308

Battin TJ, Kaplan LA, Newbold JD, Hendricks SP (2003) A mixing model analysis of stream solute dynamics and the contribution of a hyporheic zone to ecosystem function. Freshw Biol 48(6):995–1014. https://doi.org/10.1046/j.1365-2427.2003.01062.x

Battin TJ, Besemer K, Bengtsson MM, Romani AM, Packmann AI (2016) The ecology and biogeochemistry of stream biofilms. Nat Rev Microbiol 14(4):251–263. https://doi.org/10.1038/nrmicro.2016.15

Baxter CV, Hauer FR (2000) Geomorphology, hyporheic exchange, and selection of spawning habitat by bull trout (*Salvelinus confluentus*). Can J Fish Aquat Sci 57(7):1470–1481. https://doi.org/10.1139/f00-056

Berkeley Lab (2019) LBNL Watershed Function SFA East River Data Management Site. https://eastriver.pafbeta.subsurfaceinsights.com/signin. Accessed December 2019

Boano F, Demaria A, Revelli R, Ridolfi L (2010) Biogeochemical zonation due to intrameander hyporheic flow. Water Resour Res 46(2):1–13. https://doi.org/10.1029/2008WR007583

Boano F, Harvey JW, Marion A, Packman AI, Revelli R, Ridolfi L, Wörman A (2014) Hyporheic flow and transport processes: mechanisms, models, and biogeochemical implications. Rev Geophys 52(4):603–679. https://doi.org/10.1029/2011WR011784

Boulton AJ, Findlay S, Marmonier P, Stanley EH, Valett HM (1998) The functional significance of the hyporheic zone in streams and rivers. Annu Rev Ecol Evol Syst 29(1):59–81. https://doi.org/10.1146/annurev.ecolsys.29.1.59

Bryant SR (2019) Seasonal manganese transport in the hyporheic zone of a snowmelt-dominated river (East River, Colorado). The Ohio State University, Columbus, OH

Butler BA, Ranville JF, Ross PE (2008) Observed and modeled seasonal trends in dissolved and particulate cu, Fe, Mn, and Zn in a mining-impacted stream. Water Res 42(12):3135–3145. https://doi.org/10.1016/j.watres.2008.03.004

Cameron EM (1996) Hydrogeochemistry of the Fraser River, British Columbia: seasonal variation in major and minor components. J Hydrol 182(1–4):209–225. https://doi.org/10.1016/0022-1694(95)02924-9

Cardenas MB, Wilson JL (2007) Exchange across a sediment–water interface with ambient groundwater discharge. J Hydrol 346(3–4):69–80. https://doi.org/10.1016/j.jhydrol.2007.08.019

Carroll R, Williams K (2019) Discharge data collected within the East River for the Lawrence Berkeley National Laboratory Watershed Function Science Focus Area (water years 2015–2018), Watershed Function SFA. https://doi.org/10.21952/WTR/1495380

Chafiq M, Gibert J, Claret C (1999) Interactions among sediments, organic matter, and microbial activity in the hyporheic zone of an intermittent stream. Can J Fish Aquat Sci 56:487–495. https://doi.org/10.1139/f98-208

Cherkauer KA, Lettenmaier DP (1999) Hydrologic effects of frozen soils in the upper Mississippi River basin. J Geophys Res Atmos 104(D16):19599–19610. https://doi.org/10.1029/1999jd900337

Clements WH, Brooks ML, Kashian DR, Zuellig RE (2008) Changes in dissolved organic material determine exposure of stream benthic communities to UV-B radiation and heavy metals: implications for climate change. Glob Chang Biol 14(9):2201–2214. https://doi.org/10.1111/j.1365-2486.2008.01632.x

Cuthbert MO, Mackay R (2013) Impacts of nonuniform flow on estimates of vertical streambed flux. Water Resour Res 49. https://doi.org/10.1029/2011WR01158

Danczak RE, Yabusaki SB, Williams KH, Fang Y, Hobson C, Wilkins MJ (2016) Snowmelt induced hydrologic perturbations drive dynamic microbiological and geochemical behaviors across a shallow

riparian aquifer. Front Earth Sci 4(57):1–13. https://doi.org/10.3389/feart.2016.00057

Diem D, Stumm W (1984) Is dissolved Mn2 being oxidized by O2 in absence of Mn-bacteria or surface catalysts? Geochim Cosmochim Acta 48(7):1571–1573. https://doi.org/10.1016/0016-7037(84)90413-7

Dwivedi D, Steefel CI, Arora B, Newcomer M, Moulton JD, Dafflon B, Faybishenko B, Fox P, Nico P, Spycher N, Carroll R, Williams KH (2018) Geochemical exports to river from the intrameander hyporheic zone under transient hydrologic conditions: East River mountainous watershed, Colorado. Water Resour Res 54:8456–8477. https://doi.org/10.1029/2018WR023377

Elliott AH, Brooks NH (1997) Transfer of nonsorbing solutes to a streambed with bed forms: laboratory experiments. Water Resour Res 33(1):137–151. https://doi.org/10.1029/96wr02783

Emerson D (2000) Microbial oxidation of Fe(II) and Mn(II) at circumneutral pH. Environ Microbe-Metal Interact. https://doi.org/10.1128/9781555818098.ch2

Emerson D, Moyer C (1997) Isolation and characterization of novel iron-oxidizing bacteria that grow at circumneutral pH. Appl Environ Microbiol 63(12):4784–4792. https://www.ncbi.nlm.nih.gov/pmc/articles/PMC168801/. Accessed March 2020

Fellman JB, Hood E, D'Amore DV, Edwards RT, White D (2009) Seasonal changes in the chemical quality and biodegradability of dissolved organic matter exported from soils to streams in coastal temperate rainforest watersheds. Biogeochemistry 95(2–3):277–293. https://doi.org/10.1007/s10533-009-9336-6

Feris K, Ramsey P, Frazar C, Moore JN, Gannon JE, Holben WE (2003) Differences in hyporheic-zone microbial community structure along a heavy-metal contamination gradient. Appl Environ Microbiol 69(9):5563–5573. https://doi.org/10.1128/aem.69.9.5563-5573.2003

Fischer H, Kloep F, Wilzcek S, Pusch MT (2005) A rivers liver: microbial processes within the hyporheic zone of a large lowland river. Biogeochemistry 76(2):349–371. https://doi.org/10.1007/s10533-005-6896-y

Fuller CC, Harvey JW (2000) Reactive uptake of trace metals in the hyporheic zone of a mining-contaminated stream, Pinal Creek, Arizona. Environ Sci Technol 34(7):1150–1155. https://doi.org/10.1021/es990714d

Fuller CC, Bargar JR (2014) Processes of zinc attenuation by biogenic manganese oxides forming in the hyporheic zone of Pinal Creek, Arizona. Environ Sci Technol 48(4):2165–2172. https://doi.org/10.1021/es402576f

Gaskill DL, Mutschler FE, Kramer JH, Thomas JA, Zahony SG (1991) Geologic map of the Gothic quadrangle, Gunnison County, Colorado. US Geologic Survey. https://doi.org/10.3133/gq1689

Gordon RP, Lautz LK, Briggs MA, McKenzie JM (2012) Automated calculation of vertical pore-water flux from field temperature time series using the VFLUX method and computer program. J Hydrol 420:142–158. https://doi.org/10.1016/j.jhydrol.2011.11.053

Grant SB, Stewardson MJ, Marusic I (2012) Effective diffusivity and mass flux across the sediment–water interface in streams. Water Resour Res 48(5):1–16. https://doi.org/10.1029/2011WR011148

Grøn C, Tørsløv J, Albrechtsen H, Jensen HM (1992) Biodegradability of dissolved organic carbon in groundwater from an unconfined aquifer. Sci Total Environ 117–118:241–251. https://doi.org/10.1016/0048-9697(92)90091-6

Gu C, Hornberger GM, Mills AL, Herman JS (2007) Nitrate reduction in streambed sediments: effects of flow and biogeochemical kinetics. Water Resour Res 43(12):1–10. https://doi.org/10.1029/2007WR006027

Guillemette F, Giorgio PA (2011) Reconstructing the various facets of dissolved organic carbon bioavailability in freshwater ecosystems. Limnol Oceanogr 56(2):1–15. https://doi.org/10.4319/lo.2011.56.2.0734

Harte J, Saleska SR, Levy C (2015) Convergent ecosystem responses to 23-year ambient and manipulated warming link advancing snowmelt and shrub encroachment to transient and long-term climate-soil carbon feedback. Glob Chang Biol 21(6):2349–2356. https://doi.org/10.1111/gcb.12831

Harvey JW, Bencala KE (1993) The effect of streambed topography on surface–subsurface water exchange in mountain catchments. Water Resour Res 29(1):89–98. https://doi.org/10.1029/92wr01960

Harvey JW, Fuller CC (1998) Effect of enhanced manganese oxidation in the hyporheic zone on basin-scale geochemical mass balance. Water Resour Res 34(4):623–636. https://doi.org/10.1029/97WR03606

Harvey JW, Conklin MH, Koelsch RS (2003) Predicting changes in hydrologic retention in an evolving semi-arid alluvial stream. Adv Water Resour 26(9):939–950. https://doi.org/10.1016/S0309-1708(03)00085-X

Hem JD (1981) Rates of manganese oxidation in aqueous systems. Geochim Cosmochim Acta 45(8):1369–1374. https://doi.org/10.1016/0016-7037(81)90229-5

Hendricks SP (1996) Bacterial biomass, activity, and production within the hyporheic zone of a north-temperate stream. Arch Hydrobiol 136(4):467–487

Hester ET, Cardenas MB, Haggerty R, Apte SV (2017) The importance and challenge of hyporheic mixing. Water Resour Res 53:3565–3575. https://doi.org/10.1002/2016WR020005

Holmes DE, Giloteaux L, Barlett M, Chavan MA, Smith JA, Williams KH, Wilkins M, Long P, Lovley DR (2012a) Molecular analysis of the in situ growth rates of subsurface Geobacter species. Appl Environ Microbiol 79(5):1646–1653. https://doi.org/10.1128/AEM.03263-12

Holmes RM, McClelland JW, Peterson BJ, Tank SE, Bulygina E, Eglinton TI, Gordeev VV, Gurtovaya TY, Raymond PA, Repeta DJ, Staples R (2012b) Seasonal and annual fluxes of nutrients and organic matter from large rivers to the Arctic Ocean and surrounding seas. Estuaries Coast 35(2):369–382. https://doi.org/10.1007/s12237-011-9386-6

Hopkinson CS, Buffam I, Hobbie J, Vallino J, Perdue M, Eversmeyer B, Prahl F, Covert J, Hodson R, Moran MA, Smith E (1998) Terrestrial inputs of organic matter to coastal ecosystems: an intercomparison of chemical characteristics and bioavailability. Biogeochemistry 43(3):211–234. https://doi.org/10.1023/A:1006016030299

Hou Z, Nelson WC, Stegen JC, Murray CJ, Arntzen E, Crump AR, Kennedy DW, Perkins MC, Scheibe TD, Fredrickson JK, Zachara JM (2017) Geochemical and microbial community attributes in relation to hyporheic zone geological facies. Sci Rep 7(12006). https://doi.org/10.1038/s41598-017-12275-w

Ingebritsen SE, Ward ES (1998) Groundwater in geologic processes. Cambridge Univ. Press, New York

Irvine DJ, Lautz LK, Briggs MA, Gordon RP, McKenzie JM (2015) Experimental evaluation of the applicability of phase, amplitude, and combined methods to determine water flux and thermal diffusivity from temperature time series using VFLUX 2. J Hydrol 531:728–737. https://doi.org/10.1016/j.jhydrol.2015.10.054

Jin Q, Bethke CM (2003) A new rate law describing microbial respiration. Appl Environ Microbiol 69(4):2340–2348. https://doi.org/10.1128/AEM.69.4.2340-2348.2003

Kalousová K, Souček O, Tobie G, Choblet G, Čadek O (2014) Ice melting and downward transport of meltwater by two-phase flow in Europas ice shell. J Geophys Res: Planet 119(3):532–549. https://doi.org/10.1002/2013je004563

Kaplan LA, Bott TL (1989) Diel fluctuations in bacterial activity on streambed substrata during vernal algal blooms: effects of temperature, water chemistry, and habitat. Limnol Oceanogr 34(4):718–733. https://doi.org/10.4319/lo.1989.34.4.0718

Kay JT, Conklin MH, Fuller CC, O'Day PA (2001) Processes of nickel and cobalt uptake by a manganese oxide forming sediment in Pinal

Creek, Globe Mining District, Arizona. Environ Sci Technol 35(24): 4719–4725. https://doi.org/10.1021/es010514d

Knights D, Sawyer AH, Barnes RT, Musial CT, Bray S (2017) Tidal controls on riverbed denitrification along a tidal freshwater zone. Water Resour Res 53(1):799–816. https://doi.org/10.1002/2016wr019405

Koch FW, Voytek EB, Day-Lewis FD, Healy R, Briggs MA, Lane JW Jr, Werkema D (2015) 1DTempPro V2: new features for inferring groundwater/surface-water exchange. Groundw. 54(3):434–439. https://doi.org/10.1111/gwat.12369

Lapham WW (1989) Use of temperature profiles beneath streams to determine rates of vertical ground-water flow and vertical hydraulic conductivity. US Geol Surv Water Suppl Pap 2337

LaRowe DE, Van Cappellen P (2011) Degradation of natural organic matter: a thermodynamic analysis. Geochim Cosmochim Acta 75(8):2030–2042. https://doi.org/10.1016/j.gca.2011.01.020

Lensing HJ, Vogt M, Herrling B (1994) Modeling of biologically mediated redox processes in the subsurface. J Hydrol 159(1–4):125–143. https://doi.org/10.1016/0022-1694(94)90252-6

Li L, Steefel CI, Kowalsky MB, Englert A, Hubbard SS (2010) Effects of physical and geochemical heterogeneities on mineral transformation and biomass accumulation during biostimulation experiments at rifle, Colorado. J Contam Hydrol 112(1–4):45–63. https://doi.org/10.1016/j.jconhyd.2009.10.006

Liang C, Das K, Mcclendon R (2003) The influence of temperature and moisture contents regimes on the aerobic microbial activity of a biosolids composting blend. Bioresour Technol 86(2):131–137. https://doi.org/10.1016/s0960-8524(02)00153-0

Liu RZ, Zhang K, Zhang ZJ, Borthwick AG (2016) Watershed-scale environmental risk assessment of accidental water pollution: the case of Laoguan River, China. J Environ Inf 31(2):87–96. https://doi.org/10.3808/jei.201600346

Lock MA, Wallace RR, Costerton JW, Ventullo RM, Charlton SE (1984) River Epilithon: toward a structural-functional model. Oikos 42(1): 10–22. https://doi.org/10.2307/3544604

Lyons WB, Tyler SW, Gaudette HE, Long DT (1995) The use of strontium isotopes in determining groundwater mixing and brine fingering in a playa spring zone, Lake Tyrrell, Australia. J Hydrol 167(1–4):225–239. https://doi.org/10.1016/0022-1694(94)02601-7

Malenda HF (2018) From grain to floodplain: evaluating heterogeneity of floodplain hydrostratigraphy using sedimentology, geophysics, and remote sensing. Colorado School of Mines, Arthur Lakes Library, Golden, CO

Manamsa K, Lapworth DJ, Stuart ME (2016) Temporal variability of micro-organic contaminants in lowland chalk catchments: new insights into contaminant sources and hydrological processes. Sci Total Environ 568:566–577. https://doi.org/10.1016/j.scitotenv.2016.01.146

Mann PJ, Davydova A, Zimov N, Spencer RGM, Davydov S, Bulygina E, Zimov S, Holmes RM (2012) Controls on the composition and lability of dissolved organic matter in Siberia's Kolyma River basin. J Geophys Res Biogeosci 117(G1):1–15. https://doi.org/10.1029/2011JG001798

Marmonier P, Fontvieille D, Gibert J, Vanek V (1995) Distribution of dissolved organic carbon and bacteria at the interface between the Rhône River and its alluvial aquifer. J N Am Benthol Soc 14(3): 382–392. https://doi.org/10.2307/1467204

Mendoza-Lera C, Frossard A, Knie M, Federlein LL, Gessner MO, Mutz M (2017) Importance of advective mass transfer and sediment surface area for streambed microbial communities. Freshw Biol 62(1): 133–145. https://doi.org/10.1111/fwb.12856

Morrison SJ, Goodknight CS, Tigar AD, Bush RP, Gil A (2012) Naturally occurring contamination in the Mancos shale. Environ Sci Technol 46(3):1379–1387. https://doi.org/10.1021/es203211z

Mulholland PJ, DeAngelis DL (2000) Surface-subsurface exchange and nutrient spiraling, chap 6. In: Streams and ground waters. Academic. https://doi.org/10.1016/B978-012389845-6/50007-7

Nelson AR, Sawyer AH, Gabor RS, Saup CM, Bryant SR, Harris KD, Briggs MA, Williams KH, Wilkins MJ (2019) Heterogeneity in hyporheic flow, pore water chemistry, and microbial community composition in an alpine streambed. J Geophys Res Biogeosci. https://doi.org/10.1029/2019JG005226

O'Donnell JA, Aiken GR, Kane ES, Jones JB (2010) Source water controls on the character and origin of dissolved organic matter in streams of the Yukon River basin, Alaska. J Geophys Res 115(G3):1–12. https://doi.org/10.1029/2009jg001153

O'Connor BL, Harvey JW (2008) Scaling hyporheic exchange and its influence on biogeochemical reactions in aquatic ecosystems. Water Resour Res 44(12):1–17. https://doi.org/10.1029/2008WR007160

Pai H, Malenda HF, Briggs MA, Singha K, González-Pinzón R, Gooseff MN, Tyler SW (2017) Potential for small unmanned aircraft systems applications for identifying groundwater–surface water exchange in a meandering river reach. Geophys Res Lett 44(23). https://doi.org/10.1002/2017GL075836

Pallud C, Van Cappellen P (2006) Kinetics of microbial sulfate reduction in estuarine sediments. Geochim Cosmochim Acta 70(5):1148–1162. https://doi.org/10.1016/j.gca.2005.11.002

Palmer MR, Edmond JM (1989) The strontium isotope budget of the modern ocean. Earth Planet Sci Lett 92(1):11–26. https://doi.org/10.1016/0012-821X(89)90017-4

Pederson GT, Gray ST, Ault T, Marsh W, Fagre DB, Bunn AG, Woodhouse CA, Graumlich LJ (2011) Climatic controls on the snowmelt hydrology of the northern Rocky Mountains. J Clim 24(6):1666–1687. https://doi.org/10.1175/2010jcli3729.1

Peralta-Maraver I, Reiss J, Robertson AL (2018) Interplay of hydrology, community ecology and pollutant attenuation in the hyporheic zone. Sci Total Environ 610:267–275. https://doi.org/10.1016/j.scitotenv.2017.08.036

Raymond PA, McClelland JW, Holmes RM, Zhulidov AV, Mull K, Peterson BJ, Striegl RG, Aiken GR, Gurtovaya TY (2007) Flux and age of dissolved organic carbon exported to the Arctic Ocean: a carbon isotopic study of the five largest arctic rivers. Glob Biogeochem Cycles 21(4):1–9. https://doi.org/10.1029/2007GB002934

Raymond PA, Saiers JE, Sobczak WV (2016) Hydrological and biogeochemical controls on watershed dissolved organic matter transport: pulse-shunt concept. Ecology 97(1):5–16. https://doi.org/10.1890/14-1684.1

Rifai HS, Bedient PB (1990) Comparison of biodegradation kinetics with an instantaneous reaction model for groundwater. Water Resour Res 26(4):637–645. https://doi.org/10.1029/WR026i004p00637

Robbins EI, Corley TL (2005) Microdynamics and seasonal changes in manganese oxide epiprecipitation in Pinal Creek, Arizona. Hydrobiol. 534(1–3):165–180. https://doi.org/10.1007/s10750-004-1503-0

Rood SB, Pan J, Gill KM, Franks CG, Samuelson GM, Shepherd A (2008) Declining summer flows of Rocky Mountain rivers: changing seasonal hydrology and probable impacts on floodplain forests. J Hydrol 349(3–4):397–410. https://doi.org/10.1016/j.jhydrol.2007.11.012

Saup C, Bryant S, Nelson A, Harris K, Sawyer A, Christensen J, Tfaily M, Williams K, Wilkins M (2019) Depth-resolved seasonal porewater chemistry measurements from 3 locations around Meander A of the East River, Colorado. https://doi.org/10.15485/1504779

Sawyer AH (2015) Enhanced removal of groundwater-borne nitrate in heterogeneous aquatic sediments. Geophys Res Lett 42:403–410. https://doi.org/10.1002/2014GL062234

Schäffner F, Merten D, Pollok K, Wagner S, Knoblauch S, Langenhorst F, Büchel G (2015) Fast formation of supergene Mn oxides/hydroxides

under acidic conditions in the oxic/anoxic transition zone of a shallow aquifer. Environ Sci Pollut Res 22(24):19362–19375. https://doi.org/10.1007/s11356-015-4404-z

Schallenberg M, Kalff J (1993) The ecology of sediment bacteria in lakes and comparisons with other aquatic ecosystems. Ecol. 74(3):919–934. https://doi.org/10.2307/1940816

Schindler JE, Krabbenhoft DP (1998) The hyporheic zone as a source of dissolved organic carbon and carbon gases to a temperate forested stream. Biogeochemistry 43(2):157–174. https://doi.org/10.1023/A:1006005311257

Shen HW, Fehlman HM, Mendoza C (1990) Bed form resistances in open channel flows. J Hydraul Eng 116(6):799–815. https://doi.org/10.1061/(asce)0733-9429(1990)116:6(799)

Shiller AM, Stephens TH (2005) Microbial manganese oxidation in the lower Mississippi River: methods and evidence. Geomicrobiol J 22(3–4):117–125. https://doi.org/10.1080/01490450590945924

Sobczak WV, Findlay S (2002) Variation in bioavailability of dissolved organic carbon among stream hyporheic flowpaths. Ecol. 83(11):3194–3209. https://doi.org/10.1890/0012-9658(2002)083[3194:VIBODO]2.0.CO;2

Spahr NE, Boulger RW, Szmajter RJ (2000) Water quality at basic fixed sites in the upper Colorado River basin National Water-Quality Assessment study unit, October 1995–September 1998. US Geological Survey, Reston, VA

Spencer RG, Aiken GR, Wickland KP, Striegl RG, Hernes PJ (2008) Seasonal and spatial variability in dissolved organic matter quantity and composition from the Yukon River basin, Alaska. Glob Biogeochem Cycles 22(4):1–13. https://doi.org/10.1029/2008GB003231

Spencer RG, Aiken GR, Butler KD, Dornblaser MM, Striegl RG, Hernes PJ (2009) Utilizing chromophoric dissolved organic matter measurements to derive export and reactivity of dissolved organic carbon exported to the Arctic Ocean: a case study of the Yukon River, Alaska. Geophys Res Lett 36(6):1–6. https://doi.org/10.1029/2008GL036831

Stanford JA, Ward JV (1988) The hyporheic habitat of river ecosystems. Nat. 335(6185):64–66. https://www.nature.com/articles/335064a0

Stewart IT (2009) Changes in snowpack and snowmelt runoff for key mountain regions. Hydrol Process 23(1):78–94. https://doi.org/10.1002/hyp.7128

Stewart BW, Capo RC, Chadwick OA (1998) Quantitative strontium isotope models for weathering, pedogenesis and biogeochemical cycling. Geoderma 82(1–3):173–195. https://doi.org/10.1016/S0016-7061(97)00101-8

Stone RS, Dutton EG, Harris JM, Longenecker D (2002) Earlier spring snowmelt in northern Alaska as an indicator of climate change. J Geophys Res Atmos 107(D10):1468–1486. https://doi.org/10.1111/j.1365-2427.2004.01284.x

Storey RG, Williams DD (2004) Spatial responses of hyporheic invertebrates to seasonal changes in environmental parameters. Freshw Biol 49(11):1468–1486. https://doi.org/10.1111/j.1365-2427.2004.01284.x

Striegl RG, Aiken GR, Dornblaser MM, Raymond PA, Wickland KP (2005) A decrease in discharge-normalized DOC export by the Yukon River during summer through autumn. Geophys Res Lett 32(21):1–4. https://doi.org/10.1029/2005GL024413

Tebo BM, Emerson S (1986) Microbial manganese(II) oxidation in the marine environment: a quantitative study. Biogeochemistry 2(2):149–161. https://doi.org/10.1007/BF02180192

Theobald DM, Gosnell H, Riebsame WE (1996) Land use and landscape change in the Colorado Mountains II: a case study of the East River Valley. Mountain Res Dev 16(4):407–418. https://doi.org/10.2307/3673990

Triska FJ, Kennedy VC, Avanzino RJ, Zellweger GW, Bencala KE (1989) Retention and transport of nutrients in a third-order stream in northwestern California: hyporheic processes. Ecol. 70(6):1893–1905. https://doi.org/10.2307/1938120

Triska FJ, Duff JH, Avanzino RJ (1993) The role of water exchange between a stream channel and its hyporheic zone in nitrogen cycling at the terrestrial–aquatic interface. Hydrobiologia 251(1–3):167–184. https://doi.org/10.1007/BF00007177

Van Gestel M, Ladd JN, Amato M (1992) Microbial biomass responses to seasonal change and imposed drying regimes at increasing depths of undisturbed topsoil profiles. Soil Biol Biochem 24(2):103–111. https://doi.org/10.1016/0038-0717(92)90265-Y

Vano JA, Das T, Lettenmaier DP (2012) Hydrologic sensitivities of Colorado River runoff to changes in precipitation and temperature. J Hydrometeorol 13(3):932–949. https://doi.org/10.1175/jhm-d-11-069.1

Voermans JJ, Ghisalberti M, Ivey GN (2018) A model for mass transport across the sediment–water interface. Water Resour Res 54(4):2799–2812. https://doi.org/10.1002/2017WR022418

Wallace C (2019) Surface water–groundwater exchange and its effect on nitrogen transformation in the tidal freshwater zone. PhD Thesis, Ohio State University, Columbus, OH, USA

Weatherill JJ, Atashgahi S, Schneidewind U, Krause S, Ullah S, Cassidy N, Rivett MO (2018) Natural attenuation of chlorinated ethenes in hyporheic zones: a review of key biogeochemical processes and in-situ transformation potential. Water Res 128:362–382. https://doi.org/10.1016/j.watres.2017.10.059

Winnick MJ, Carroll RW, Williams KH, Maxwell RM, Dong W, Maher K (2017) Snowmelt controls on concentration–discharge relationships and the balance of oxidative and acid-base weathering fluxes in an alpine catchment, East River, Colorado. Water Resour Res 53(3):2507–2523. https://doi.org/10.1002/2016WR019724

Wondzell SM (2011) The role of the hyporheic zone across stream networks. Hydrol Process 25(22):3525–3532. https://doi.org/10.1002/hyp.8119

Wong JC, Williams DD (2009) Sources and seasonal patterns of dissolved organic matter (DOM) in the hyporheic zone. Hydrobiologia 647(1):99–111. https://doi.org/10.1007/s10750-009-9950-2

Xu F, Liu Y, Zachara J, Bowden M, Kennedy D, Plymale AE, Liu C (2017) Redox transformation and reductive immobilization of Cr (VI) in the Columbia River hyporheic zone sediments. J Hydrol 555:278–287. https://doi.org/10.1016/j.jhydrol.2017.10.016

Zarnetske JP, Haggerty R, Wondzell SM, Bokil VA, González-Pinzón R (2012) Coupled transport and reaction kinetics control the nitrate source-sink function of hyporheic zones. Water Resour Res 48(11):1–15. https://doi.org/10.1029/2012WR011894

Zelles L, Adrian P, Bai Q, Stepper K, Adrian M, Fischer K, Ziegler A (1991) Microbial activity measured in soils stored under different temperature and humidity conditions. Soil Biol Biochem 23(10):955–962. https://doi.org/10.1016/0038-0717(91)90176-k